Loss of nuclear DNA ligase III reverts PARP inhibitor resistance in BRCA1/53BP1 double-deficient cells by exposing ssDNA gaps

Mariana Paes Dias[1,12,13], **Vivek Tripathi**[2,13], **Ingrid van der Heijden**[1,12], **Ke Cong**[3], **Eleni-Maria Manolika**[2], **Jinhyuk Bhin**[1,5,12], **Ewa Gogola**[1,12], **Panagiotis Galanos**[4], **Stefano Annunziato**[1,12], **Cor Lieftink**[5], **Miguel Andújar-Sánchez**[6], **Sanjiban Chakrabarty**[7], **Graeme C.M. Smith**[8], **Marieke van de Ven**[9], **Roderick L. Beijersbergen**[5], **Jirina Bartkova**[4,10], **Sven Rottenberg**[1,11], **Sharon Cantor**[3], **Jiri Bartek**[4,10], **Arnab Ray Chaudhuri**[2,*], **Jos Jonkers**[1,12,14,*]

[1]Division of Molecular Pathology, the Netherlands Cancer Institute, 1066CX Amsterdam, the Netherlands

[2]Department of Molecular Genetics, Erasmus MC Cancer Institute, Erasmus University Medical Center, 3015GD Rotterdam, the Netherlands

[3]Department of Molecular, Cell and Cancer Biology, University of Massachusetts Medical School, Worcester, MA 01605, USA

[4]Genome Integrity Unit, Danish Cancer Society Research Center, Copenhagen 2100, Denmark

[5]Robotics and Screening Center, Division of Molecular Carcinogenesis, the Netherlands Cancer Institute, 1066CX Amsterdam, the Netherlands

[6]Pathology Department, Complejo Hospitalario Universitario Insular, Las Palmas, Gran Canaria, Spain

[7]Department of Cell and Molecular Biology, Manipal School of Life Sciences, Manipal Academy of Higher Education, Karnataka 576104, India

[8]Artios Pharma, Glenn Berge Building, Babraham Research Campus, Cambridge CB22 3FH, UK

[9]Mouse Clinic for Cancer and Aging, Preclinical Intervention Unit, the Netherlands Cancer Institute, 1066CX Amsterdam, the Netherlands

[10]Karolinska Institutet, Department of Medical Biochemistry and Biophysics, Division of Genome Biology, Science for Life Laboratory, Stockholm 171 77, Sweden

[11]Institute of Animal Pathology, Vetsuisse Faculty, University of Bern, Bern 3012, Switzerland

*Correspondence: a.raychaudhuri@erasmusmc.nl (A.R.C.), j.jonkers@nki.nl (J.J.).

[12]Oncode Institute, 1066CX Amsterdam, the Netherlands

[13]These authors contributed equally

[14]Lead contact

SUMMARY

Inhibitors of poly(ADP-ribose) (PAR) polymerase (PARPi) have entered the clinic for the treatment of homologous recombination (HR)-deficient cancers. Despite the success of this approach, preclinical and clinical research with PARPi has revealed multiple resistance mechanisms, highlighting the need for identification of novel functional biomarkers and combination treatment strategies. Functional genetic screens performed in cells and organoids that acquired resistance to PARPi by loss of 53BP1 identified loss of LIG3 as an enhancer of PARPi toxicity in BRCA1-deficient cells. Enhancement of PARPi toxicity by LIG3 depletion is dependent on BRCA1 deficiency but independent of the loss of 53BP1 pathway. Mechanistically, we show that LIG3 loss promotes formation of MRE11-mediated post-replicative ssDNA gaps in BRCA1-deficient and BRCA1/53BP1 double-deficient cells exposed to PARPi, leading to an accumulation of chromosomal abnormalities. LIG3 depletion also enhances efficacy of PARPi against BRCA1-deficient mammary tumors in mice, suggesting LIG3 as a potential therapeutic target.

Graphical Abstract
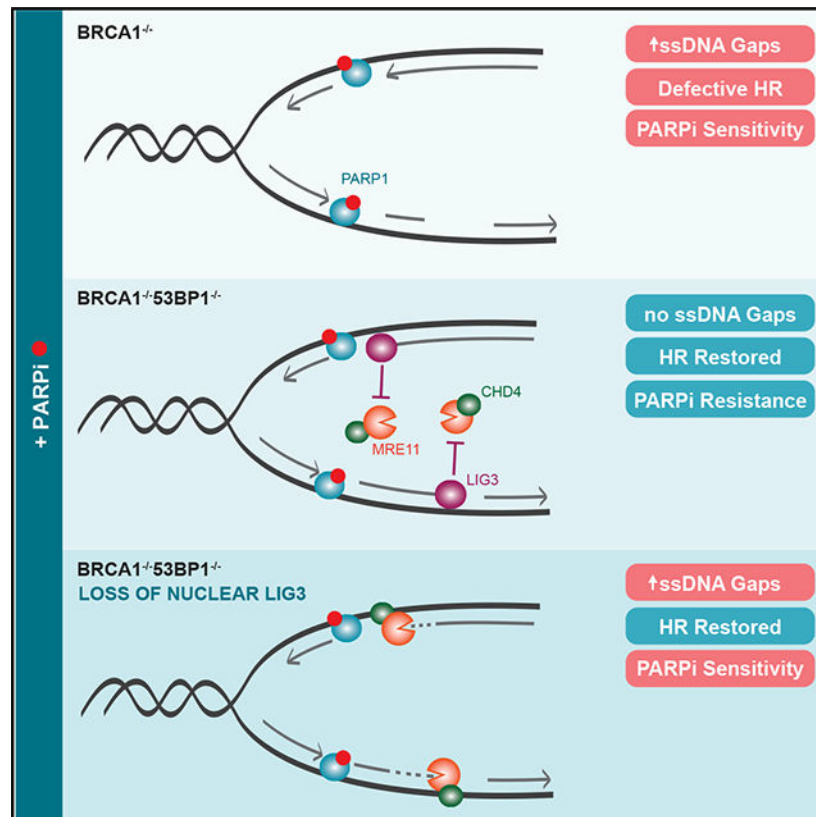
In brief

Paes Dias et al. report that loss of nuclear LIG3 increases PARPi toxicity in BRCA1/53BP1 double-deficient cells by promoting the formation of MRE11-mediated post-replicative ssDNA gaps, leading to accumulation of chromosomal abnormalities. LIG3 depletion also enhances the efficacy of PARPi against BRCA1-deficient mammary tumors in mice, suggesting LIG3 as a potential therapeutic target.

INTRODUCTION

Defects in DNA repair result in genome instability and thereby contribute to the development and progression of cancer. Alterations in high-fidelity DNA repair genes lead to a greater reliance on compensatory error-prone repair pathways for cellular survival. This not only results in the accumulation of tumor-promoting mutations but also provides cancer-specific vulnerabilities that can be exploited for targeted cancer therapy. The first example of such targeted approach was the use of poly(ADP-ribose) polymerase (PARP) inhibitors (PARPi) in the treatment of *BRCA1*- or *BRCA2*-deficient tumors defective in the error-free repair of DNA double-strand breaks (DSBs) through homologous recombination (HR) (Bryant et al., 2005; Farmer et al., 2005).

PARP1, which is the main target for PARPi, is involved in various cellular processes, including the sensing of DNA single-strand breaks (SSBs), repair of DNA DSBs, stabilization of replication forks (RFs), chromatin remodeling (reviewed by Ray Chaudhuri and Nussenzweig, 2017), and the sensing of unligated Okazaki fragments during DNA replication (Hanzlikova et al., 2018). Upon DNA damage, PARP1 is rapidly recruited to sites of DNA damage, where it post-translationally modifies substrate proteins by synthesizing poly(ADP-ribose) (PAR) chains via PARylation. PARP1 itself is also a target of PARylation, and the resulting PAR chains serve to recruit downstream repair factors. AutoPARylation of PARP1 also enhances its release from DNA, which is essential for various DNA repair processes (Pascal and Ellenberger, 2015).

PARPi act not only through catalytic inhibition of PARP1 but also via trapping of PARP1 onto chromatin, resulting in RF collapse (Helleday, 2011; Murai et al., 2012, 2014). PARPi-treated *BRCA1/2*-defective cells can only use error-prone repair to resolve DSBs caused by RF collapse, resulting in accumulation of chromosomal aberrations and cell death by mitotic catastrophe (Lupo and Trusolino, 2014). Successful clinical trials have resulted in approval of PARPi for treatment of patients with *BRCA1/2* mutant ovarian and breast cancers (Paes Dias et al., 2021).

Despite the success of PARPi, multiple mechanisms of resistance have been identified, including upregulation of drug efflux transporters (Rottenberg et al., 2008); PARP1 downregulation, inactivation, or mutation (Pettitt et al., 2018); loss of PAR glycohydrolase (Gogola et al., 2018); or restoration of RF protection in the absence of BRCA1/2 (Ray Chaudhuri et al., 2016). However, the best-studied PARPi resistance mechanisms involve restoration of HR activity via re-activation of BRCA1/2 function or via loss of factors that govern DSB end-protection in BRCA1-deficient cells (Paes Dias et al., 2021). The

latter may be achieved by loss of components of the 53BP1-RIF1-REV7-Shieldin complex (Boersma et al., 2015; Bouwman et al., 2010; Bunting et al., 2010; Chapman et al., 2013; Dev et al., 2018; Escribano-Díaz et al., 2013; Ghezraoui et al., 2018; Noordermeer et al., 2018; Xu et al., 2015).

Importantly, drug resistance often comes at a fitness cost due to collateral vulnerabilities, which can be exploited therapeutically. For example, PARG inactivation causes PARPi resistance but results in increased sensitivity to ionizing radiation (IR) and temozolomide (Gogola et al., 2018). Similarly, BRCA1-deficient tumors that acquired PARPi resistance via 53BP1 loss are more radiosensitive (Barazas et al., 2019). In this study, we identified DNA ligase III (LIG3), a known DNA repair factor (Caldecott et al., 1996; Cappelli et al., 1997; Simsek et al., 2011; Wang et al., 2005), as a collateral vulnerability of BRCA1-deficient cells with acquired PARPi resistance due to loss of DSB end-protection.

RESULTS

Functional genetic dropout screens identify LIG3 as a modulator of PARPi resistance in BRCA1/53BP1 double-deficient cells

To identify acquired vulnerabilities in BRCA1-deficient cells that developed PARPi resistance via BRCA1-independent restoration of HR, we carried out functional genetic dropout screens in two types of cellular models deficient for BRCA1, p53, and 53BP1. The first screen was performed in genetically well-defined $Brca1^{-/-};Trp53^{-/-};Trp53bp1^{-/-}$ mouse embryonic stem cells (ES-B1P.R mESCs) (Figure S1A). The second screen was performed in $Brca1^{-/-};Trp53^{-/-};Trp53bp1^{-/-}$ tumor organoids (ORG-KB1P.R), derived from a $K14cre;Brca1^{F/F};Trp53^{F/F}$ (KB1P) mouse mammary tumor that acquired resistance to PARPi *in vivo* because of loss of 53BP1 function (Duarte et al., 2018) (Figure S1A). Both cellular models were transduced with a lentiviral library of 1,976 short hairpin RNA (shRNA) constructs targeting 391 DNA damage response (DDR)-related genes (Gogola et al., 2018; Xu et al., 2015). Cells were either mock-treated or selected for 3 weeks in the presence of the PARPi olaparib (Figure 1A). Olaparib selection was carried out at 25 nM in ES-B1P.R mESCs and 50 nM in ORG-KB1P.R organoids, concentrations that do not affect the viability of resistant cells but are lethal to the corresponding PARPi-sensitive cells. Sequencing of the shRNAs in the surviving cells revealed a specific and reproducible dropout of hairpins targeting *Lig3* in the olaparib-treated cell population in both ES-B1P.R mESCs and ORG-KB1P.R organoids (Figures 1B and S1B; Table S1). Furthermore, *Lig3* was observed to be the only common significant dropout gene identified across both screens (Figure 1C). We therefore decided to investigate further whether LIG3 would constitute a useful target for the reversion of PARPi resistance in BRCA1-deficient cells.

Depletion of LIG3 increases sensitivity to PARPi, independent of 53BP1 loss

To validate the findings of our shRNA screens, we carried out viability assays using shRNA-mediated depletion of LIG3 in ORG-KB1P.R organoids. LIG3 depletion significantly increased sensitivity to olaparib compared with the parental cells (Figures 1D and S1C). Increased sensitivity to olaparib was also observed upon depletion of LIG3 in PARPi-resistant KB1P.R cells, derived from an independent PARPi-resistant KB1P tumor with

53BP1 loss (Jaspers et al., 2013) (Figures S1A, S1D, and S1E). These results confirm that depletion of LIG3 results in re-sensitization of BRCA1/53BP1 double-deficient cells to PARPi. Furthermore, depletion of LIG3 also reverted the resistance to olaparib in *Brca1*$^{-/-}$*;Trp53*$^{-/-}$ KB1P.S mammary tumor cells depleted of REV7, a downstream partner of 53BP1 (Boersma et al., 2015; Xu et al., 2015) (Figures S1A, S1F, and S1G), indicating that LIG3-mediated resistance is not exclusive for 53BP1-deficient cells.

We next asked whether LIG3 depletion would also increase the PARPi sensitivity of treatment-naive BRCA1-defcient tumor cells with functional 53BP1. To test this, we used *Brca1*$^{-/-}$*;Trp53*$^{-/-}$ organoids, hereafter referred to as ORG-KB1P.S, and KB1P.S cells derived from independent PARPi-naive KB1P tumors (Figure S1A) (Duarte et al., 2018; Jaspers et al., 2013). In both cellular models, shRNA-mediated depletion of LIG3 resulted in increased sensitivity to olaparib (Figures 1E, S1C, S1H, and S1I). Corroborating our findings, depletion of LIG3 also resulted in increased sensitivity to olaparib in the human *BRCA1* mutant breast cancer cell line SUM149PT (Figures S1J and S1K). Importantly, our results were not restricted to olaparib, as LIG3 depletion also increased the sensitivity of KB1P.S cells to the PARPi talazoparib and veliparib (Figure S1L).

PARPi sensitization of cells by LIG3 depletion is dependent on BRCA1 status

Next, we sought to investigate whether the increased PARPi sensitivity of LIG3-depleted cells is BRCA1 dependent. shRNA-mediated depletion of LIG3 in *Trp53*$^{-/-}$ organoids (ORG-KP), derived from *K14cre*;*Trp53*$^{F/F}$ (KP) mouse mammary tumors (Figure S1A) (Duarte et al., 2018), slightly increased sensitivity to PARPi, but only at a high concentration of 10 μM (Figures 1F, S2A, and S2B). To corroborate these data, we validated the effect of LIG3 depletion in *R26*^{creERT2}*;Brca1*$^{SCo/-}$*;Trp53*$^{-/-}$*;Trp53bp1*$^{-/-}$ mESCs (ES-P.R). Addition of 4-hydroxytamoxifen (4OHT) to ES-P.R mESCs induces cre-mediated deletion of the remaining *Brca1* allele, resulting in *R26*^{creERT2}*;Brca1*$^{-/-}$*;Trp53*$^{-/-}$*;Trp53bp1*$^{-/-}$ mESCs (ES-B1P.R), deficient for BRCA1 (Figures 1G and S1A) (Bouwman et al., 2010). As these mESCs are deficient for p53 and 53BP1, no difference in olaparib sensitivity was observed between the BRCA1-proficient ES-P.R and the BRCA1-deficient ES-B1P.R mESCs (Figures 1H and S2C–S2F). shRNA-mediated depletion of LIG3 did not affect cell proliferation in untreated ES-P or ES-B1P.R mESCs. However, LIG3 depletion did result in increased olaparib sensitivity in ES-B1P.R cells, compared with unmodified cells (Figures 1H, S2E, and S2F). To investigate whether the effect was independent of the loss of 53BP1, we repeated this experiment in 53BP1-proficient *R26*^{creERT2}*; Brca1*$^{SCo/-}$*;Trp53*$^{-/-}$ mESCs (ES-P) (Figures S1A, S2C, S2D, and S2G). Depletion of LIG3 increased the sensitivity to PARPi in BRCA1-deficient ES-B1P.S cells but not in BRCA1-proficient ES-P cells (Figures S2H–S2J).

Additionally, we tested depletion of LIG3 in three isogenic human TERT-immortalized retinal pigment epithelial (RPE1) cell lines with engineered loss of *TP53* (RPE1-P), *TP53+BRCA1* (RPE1-B1P.S), or *TP53+BRCA1+TP53BP1* (RPE1-B1P.R) (Figure S1A). In line with the data observed in mouse cells, shRNA-mediated depletion of LIG3 only increased sensitivity to olaparib in RPE1-P cells at a higher concentration of 1 μM, but rendered RPE1-B1P.R cells as sensitive to olaparib as the RPE1-B1P.S cells (Figures 1I,

S2K, and S2L). In addition, depletion of LIG3 further increased sensitivity of RPE1-B1P.S cells to olaparib (Figures 1I, S2K, and S2L).

Finally, we asked if loss of LIG3 also results in hypersensitization of BRCA2-deficient cells to PARPi. To test this, we used *Brca2$^{−/−}$;Trp53$^{−/−}$* (KB2P) cells derived from a *K14cre;Brca2$^{F/F}$; Trp53$^{F/F}$* (KB2P) mouse mammary tumor (Evers et al., 2008) (Figure S1A). shRNA-mediated depletion of LIG3 in KB2P cells resulted in an increase in olaparib sensitivity that was modest compared with the profound increase observed in KB1P cells (Figures S2M and S2N). In addition, we depleted LIG3 in BRCA2-proficient human DLD1 cells and an isogenic derivative in which *BRCA2* was deleted (DLD1-B2KO). We did not observe a significant increase in sensitivity to olaparib in the BRCA2-deficient DLD1-B2KO cells after depletion of LIG3 (Figures S2O and S2P). In line with the previous data, depletion of LIG3 in DLD1 cells only resulted in increased olaparib sensitivity at a high concentration of 2.5 μM (Figures S2O and S2Q). Taken together, our data show that LIG3 is a strong modulator of PARPi response specifically in BRCA1-deficient cells and that LIG3 depletion enhances the toxicity of PARPi in BRCA1-deficient cells that acquired resistance because of loss of DSB end-protection.

PARPi toxicity in LIG3-depleted cells is dependent on PARP1

Most PARPi, in addition to blocking the catalytic activity of PARP1, also induce toxic PARP1-DNA complexes as a result of their trapping capacity (Murai et al., 2012, 2014). To test whether PARPi-mediated PARP1 trapping contributes to PARPi toxicity in LIG3-depleted cells, we generated *Parp1*-knockout isogenic derivatives of ES-P.R mESCs and verified loss of PARP1 expression using western blot (Figure S3A). Compared with cells transduced with non-targeting single guide RNA (sgRNA) (ES-P.R sgNTG), ES-P.R-*Parp1$^{−/−}$* cells displayed decreased levels of PAR upon PARG inhibition and/or methyl methanesulfonate (MMS) treatment (Gogola et al., 2018), confirming functional loss of PARP1 (Figure S3B). We next exposed ES-P.R sgNTG and ES-P.R-*Parp1$^{−/−}$* cells to 4OHT to produce BRCA1-deficient ES-B1P.R sgNTG and ES-B1P.R-*Parp1$^{−/−}$* mESCs, which were tested for olaparib sensitivity with or without LIG3 depletion (Figures S3C–S3F). shRNA-mediated depletion of LIG3 did not affect viability of ES-B1P.R sgNTG or ES-B1P.R-*Parp1$^{−/−}$* cells (Figure S3E). In line with the notion that PARPi cytotoxicity is mediated by PARP1 trapping (Murai et al., 2012; Pettitt et al., 2013), elimination of PARP1 resulted in reduced sensitivity of ES-B1P.R cells to olaparib (Figure S3F). Importantly, elimination of PARP1 also reduced olaparib sensitivity in LIG3-depleted ES-B1P.R cells, indicating that the effect of LIG3 depletion on PARPi sensitivity in BRCA1-deficient cells is partially mediated by PARP1 trapping.

Resistance to PARPi in 53BP1-deficient KB1P cells is mediated by nuclear LIG3

The *LIG3* gene encodes both mitochondrial and nuclear proteins (Lakshmipathy and Campbell, 1999). Importantly, mitochondrial LIG3 is essential for cellular viability as it ensures mtDNA integrity (Puebla-Osorio et al., 2006). Consequently, complete deletion of *Lig3* results in cellular death and early embryonic lethality in mice, whereas nuclear LIG3 has been shown to be dispensable for cell viability (Simsek et al., 2011). We therefore asked whether the increased PARPi sensitivity of LIG3-depleted BRCA1-deficient cells

resulted from loss of LIG3 activity in the nucleus or in the mitochondria. To test this, we generated nuclear *Lig3*-knockout cells, which express only the mitochondrial form of LIG3. To this end, we used 53BP1-deficient KB1P.R mouse tumor cells in which we introduced an ATG > CTC mutation in the internal translation initiation site that is required for expression of the nuclear LIG3 isoform but does not affect expression of mitochondrial LIG3 (Figure 2A) (Lakshmipathy and Campbell, 1999). Western blot analysis of KB1P.R cells, one KB1P.R (LIG3$^{mut/wt}$) clone heterozygous for the ATG > CTC mutation (B1), and two KB1P.R(LIG3$^{mut/mut}$) clones with homozygous ATG > CTC mutation (A3, F5) showed that LIG3 is still expressed (Figure 2B). However, immunofluorescence analysis of LIG3 in the same clones revealed that parental KB1P.R cells and the heterozygous KB1P.R(LIG3$^{mut/wt}$) B1 clone displayed LIG3 staining in both nucleus and mitochondria, whereas the homozygous KB1P.R(LIG3$^{mut/mut}$) A3 and KB1P.R(LIG3$^{mut/mut}$) F5 clones exhibited loss of nuclear LIG3 expression (Figure 2C). Finally, we investigated whether the nuclear mutants of LIG3 displayed increased sensitivity to PARPi. Long-term clonogenic assays revealed that the nuclear LIG3-deficient KB1P.R(LIG3$^{mut/mut}$) A3 and KB1P.R(LIG3$^{mut/mut}$) F5 clones displayed hyper-sensitivity to olaparib compared with the PARPi-resistant parental KB1P.R cells and the heterozygous KB1P.R(LIG3$^{mut/wt}$) B1 clone (Figures 2D, S4A, and S4B).

Nuclear LIG3 consists of an N-terminal like zinc finger (ZnF) domain, which is required for binding to DNA secondary structures (Taylor et al., 2000), and a C-terminal BRCT domain required for interaction with other proteins such as XRCC1 (Caldecott et al., 1994). To test the role of these domains in LIG3-mediated PARPi resistance, we generated overexpression constructs for wild-type human LIG3 (hLIG3^{WT}), carrying a mutation in the PARP-like ZnF domain (hLIG3^{R31L}) or a C-terminal 774-922 truncation (hLIG3 $^{774-922}$). We introduced these constructs in KB1P.R(LIG3$^{mut/mut}$) A3 cells, hereafter referred to as KB1P.R$^{(\ nucLIG3)}$, and carried out clonogenic assays (Figures 2E). Whereas overexpression of hLIG3^{WT} rescued sensitivity to olaparib in KB1P.R$^{(\ nucLIG3)}$ cells, overexpression of either hLIG3 mutant failed to suppress olaparib sensitivity in KB1P.R$^{(\ nucLIG3)}$ cells (Figures 2F and S4C), indicating that both the DNA binding and BRCT domain are required for driving PARPi resistance in BRCA1 and 53BP1 double-deficient tumor cells.

LIG3 is required at RFs in BRCA1-deficient cells treated with PARPi

Our data indicate that the increase in sensitivity to PARPi arising from LIG3 depletion is independent of the loss of DSB end-protection, and therefore we hypothesized that this phenomenon could be independent of HR status. To test this hypothesis, we carried out RAD51 IR-induced foci (RAD51 IRIF) in our mouse tumor-derived cell lines as a readout of functional HR status (Xu et al., 2015). As expected, BRCA1-deficient KB1P.S cells had significantly less IRIF per cell than the BRCA1-proficient KP cells (Figure S1A), while the BRCA1/53BP1 double-deficient KB1P.R cells displayed increased numbers of IRIF compared with KB1P.S (Figure S5A). Moreover, KB1P.R cells with shRNA-mediated depletion of LIG3 or with deletion of LIG3 nuclear isoform did not show a significant reduction of RAD51 IRIF (Figure S5A), corroborating our hypothesis that the sensitivity observed in LIG3-depleted cells is not a result of decreased HR in these cells.

tLIG3 is also involved in the repair of DSBs by alternative end-joining (Alt-EJ) through its interaction with POLθ (Simsek et al., 2011; Wang et al., 2005). It has been previously reported that HR-deficient tumors rely on POLθ for survival and that its depletion can enhance PARPi response in both BRCA1-deficient cells and BRCA1/53BP1 double-mutant cells (Ceccaldi et al., 2015; Mateos-Gomez et al., 2015; Zhou et al., 2020). Therefore, we hypothesized that if the suppressive effect of LIG3 on PARPi sensitivity in BRCA1-deficient cells is dependent on its role in Alt-EJ, viability of LIG3-deficient cells should not be affected by inhibition of POLθ and that sensitivity of LIG3-deficient cells to olaparib would not be amplified by POLθ inhibition. To test this, we carried out both long-term clonogenic and short-term cytotoxicity assays with olaparib and the POLθ inhibitor ART558 (Zatreanu et al., 2021). Interestingly, inhibition of POLθ alone resulted in increased cell death in KB1P.R parental cells, as well as in nuclear LIG3 mutant KB1P.R$^{(nucLIG3)}$ cells (Figures S5B and S5C). Moreover, we observed a synergistic interaction between olaparib and ART558 in both cell lines (Figure S5C), suggesting that LIG3-mediated resistance is independent of its role in POLθ-mediated end-joining.

Data from recent studies indicate that LIG3 is present at RFs (Arakawa and Iliakis, 2015; Cong et al., 2021; Hanzlikova et al., 2018; Sriramachandran et al., 2020). Therefore, we next investigated whether LIG3 localizes to sites of DNA replication marked by 5-ethynyl-2′-deoxyuridine (EdU) incorporation, in the absence of DNA damage induction. To test this, we performed proximity ligation-based assays (PLA) to detect LIG3 binding to replicated DNA (Mukherjee et al., 2019; Taglialatela et al., 2017) in BRCA1-proficient KP, BRCA1-reconstituted KB1P.S+hB1 (Barazas et al., 2019), and BRCA1-deficient KB1P.S cells. Interestingly, untreated KB1P.S cells showed significantly higher levels of LIG3-EdU PLA foci than KP or KB1P.S+hB1cells (Figures 3A, 3B, S5D, and S5E). We next tested if LIG3 localization at replication sites is affected by PARPi treatments, which would trap PARP1 at RFs. Therefore, we carried out LIG3-EdU PLA after incubating cells with olaparib for 2 h. Quantification of LIG3-EdU PLA foci revealed that PARPi treatment did not induce any increase in the number of foci in KB1P.S+hB1 cells. In contrast, BRCA1-deficient KB1P.S cells displayed a striking increase in the number of PLA foci after olaparib treatment (Figures 3A and S5D). We next investigated whether LIG3 localization at replication sites is affected by the PARG inhibitor (PARGi) PDDX-001, which is known to increase PAR levels and to also result in an increase in chromatin-associated PARP1 (Gogola et al., 2018; Hanzlikova et al., 2018; James et al., 2016). We therefore carried out LIG3-EdU PLA after incubating cells with PDDX-001 for 30 min. Similar to olaparib-treated cells, PDDX-001-treated BRCA1-deficient cells showed a strong increase in the number of LIG3-EdU PLA foci, while no significant changes were observed in KP cells (Figures 3B and S5E). Co-localization of LIG3 at EdU-marked replication sites after PDDX-001 treatment was also verified qualitatively by LIG3 immunostaining in KP, KB1P.S cells and KB1P.R cells (Figure S5F). As we observe that both PARPi and PARGi treatment results in an increase in LIG3-EdU PLA foci, and that olaparib treatment results in a reduction of PAR levels while treatment with PDDX-001 results in an increase, we conclude that the upsurge in LIG3-EdU PLA is probably caused by PARP1 trapping, which is common to both inhibitors. Of note, untreated KB2P cells showed similar numbers of LIG3-EdU PLA foci as KP cells (Figures S5G and S5H). However, upon treatment with PDDX-001,

KB2P cells showed more LIG3-EdU PLA foci than KP cells but significantly fewer than KB1P.S cells (Figures S5G and S5H). These data support our previous findings that LIG3 depletion in BRCA2-deficient cells has a more modest effect on olaparib sensitivity than in BRCA1-deficient cells.

As LIG3 seems to play a role at replication sites in BRCA1-deficient conditions, we asked whether depletion of LIG3 would affect RF progression in untreated and PARPi-treated BRCA1-deficient cells. To test this, we performed DNA fiber assay in BRCA1-deficient KB1P.S and BRCA1-reconstituted KB1P.S+hB1 cells. Cells were pre-incubated with olaparib for 80 min, followed by sequential labeling with CldU (red) and IdU (green) for 20 min each in the presence of olaparib (Figure 3C). Progression was measured by tract lengths of CldU and IdU. Analysis of RF speeds revealed no significant increase in BRCA1-proficient KB1P.S+hB1 cells after olaparib treatment (Figures 3D, S5I, and S5J). In contrast, BRCA1-deficient KB1P.S cells exhibited an increase in RF speed upon olaparib treatment, in line with previous work (Cong et al., 2021). Surprisingly, while small interfering RNA (siRNA)-mediated depletion of LIG3 did not affect RF speed in untreated cells, it significantly suppressed the PARPi-induced increase in RF speed in KB1P.S cells (Figures 3D, S5I, and S5J). As observed in KB1P.S cells, olaparib treatment also resulted in increased RF speed in BRCA1/53BP1 double-deficient KB1P.R cells, which was rescued by siRNA-mediated LIG3 depletion or loss of nuclear LIG3 (Figures 3E, S5I, and S5K–S5M). Similar data were also observed in BRCA1/53BP1 double-deficient RPE1-B1P.R cells treated with PARPi (Figures S5N and S5O). As loss of LIG3 rescued the increase in RF speed in both BRCA1 and BRCA1/53BP1 double-deficient cells, we asked if this phenomenon was due to a restraint in RF speed or to continuous RF stalling and restart and thus increased replication stress. We next analyzed RF symmetry in BRCA1-proficient and BRCA1-deficient cells by measuring sister fork ratio (Figures 3F and 3G). Whereas BRCA1-proficient KB1P.S+hB1 cells did not show any significant differences in RF symmetry across conditions, depletion of LIG3 induced a significant increase in sister fork asymmetry, indicative of RF stalling, in BRCA1-deficient KB1P.S cells exposed to olaparib (Figure 3G). Similarly, loss of nuclear LIG3 in KB1P.R$^{(\text{nucLIG3})}$ cells also resulted in RF asymmetry upon olaparib treatment (Figure 3H). These data corroborate our hypothesis that the lack of PARPi-induced RF acceleration observed in LIG3-depleted cells is a result of persistent RF stress upon loss of LIG3. Overall, our results support the notion that depletion of LIG3 in BRCA1-deficient cells exposed to PARPi leads to slower and asymmetric RFs.

Loss of LIG3 in BRCA1-deficient cells results in an increase in PARPi-mediated ssDNA regions

Recent studies have suggested that accumulation of post-replicative single-stranded DNA (ssDNA) gaps underlies BRCA deficiency and PARPi sensitivity (Cong et al., 2021; Panzarino et al., 2021; Quinet et al., 2020). As LIG3 is a DNA ligase and our data indicate that it is present at active RFs in BRCA1-deficient cells, we asked whether LIG3 depletion would result in an increase in S phase-associated ssDNA. To test this, we cultured KB1P.S+hB1, KB1P.S, and KB1P.R mouse tumor cells in medium supplemented with BrdU for 48 h followed by 2 h treatment with olaparib and quantification of native BrdU

intensity by quantitative image-based cytometry (QIBC) (Toledo et al., 2013) (Figure 4A). As previously suggested, olaparib treatment did not result in an increase in ssDNA levels in BRCA1-proficient KB1P.S+hB1 cells or in BRCA1/53BP1 double-deficient KB1P.R cells (Figures 4B, 4C, S6A, and S6B). However, treatment with olaparib resulted in a significant increase in ssDNA levels in BRCA1-deficient KB1P.S cells during S phase (Figures 4B, 4C, S6A, and S6B). These results were further confirmed in the RPE1 isogenic lines, showing PARPi-induced increase in ssDNA levels in RPE1-B1P.S cells but not in RPE1-P or RPE1-B1P.R cells (Figure S6D). Importantly, deletion of nuclear LIG3 in KB1P.R cells or shRNA-mediated LIG3 depletion in RPE1-B1P.R cells restored PARPi-induced ssDNA gap accumulation (Figures 4D, S6C, and S6D). LIG3 depletion also further increased PARPi-induced ssDNA gap accumulation in RPE1-B1P.S cells (Figure S6D), suggesting that LIG3-mediated ssDNA gap suppression is HR independent.

Increase in ssDNA gaps results in increased genomic instability in LIG3-deficient cells

MRE11 has been shown to be involved in the processing of gaps at and behind RFs (Hashimoto et al., 2010; Ray Chaudhuri et al., 2016; Schlacher et al., 2011). Furthermore, the nucleosome remodeling factor CHD4 has been reported to be involved in the recruitment of MRE11 for nuclease processing at stressed RFs (Ray Chaudhuri et al., 2016). We therefore tested if the PARPi-induced increase in replication-associated ssDNA regions in KB1P.S and KB1P.R$^{(\text{nucLIG3})}$ cells was dependent on either MRE11 or CHD4. Both inhibition of MRE11 with mirin and siRNA-mediated depletion of CHD4 rescued the increase in replication-associated ssDNA regions in KB1P.R$^{(\text{nucLIG3})}$ cells treated with olaparib (Figures 5A and S6E–S6G). In contrast, neither treatment with mirin nor depletion of CHD4 rescued ssDNA exposure in parental KB1P.S cells (Figures 5A, S6F, and S6G). To confirm if the observed increase of ssDNA was in the vicinity of RFs, we used electron microscopy (EM) to visualize the fine architecture of replication intermediates in KB1P.S, KB1P.R, and KB1P.R$^{(\text{nucLIG3})}$ cells after 2 h treatment with olaparib (Figures 5B and 5C). In untreated conditions, a minority of the DNA molecules displayed ssDNA gaps behind the RF in all the three cell lines analyzed. However, olaparib treatment markedly enhanced the percentage of molecules displaying one or more post-replicative ssDNA gaps, specifically in KB1P.S and KB1P.R$^{(\text{nucLIG3})}$ but not in KB1P.R cells (Figure 5D). Consistent with our QIBC data, we observed that the PARPi-induced post-replicative gaps in KB1P.S cells were not rescued upon inhibition of MRE11, whereas the post-replicative gaps in olaparib-treated KB1P.R$^{(\text{nucLIG3})}$ cells were dependent on MRE11-mediated processing (Figure 5D). Of note, we did not observe an increase in RF reversal in any of the conditions (Figure S6H). Taken together, these data suggest that the PARPi-induced ssDNA regions in BRCA1-deficient and 53BP1-proficient cells are distinct in nature from the PARPi-induced gaps generated upon loss of LIG3 in BRCA1/53BP1 double-deficient cells.

We next questioned if the suppression of post-replicative gaps observed upon either MRE11 inhibition or depletion of CHD4 could result in RF stability in KB1P.R$^{(\text{nucLIG3})}$ cells. To assess this, we performed DNA fiber assays to measure RF asymmetry in KB1P.R and KB1P.R$^{(\text{nucLIG3})}$ cells upon exposure to olaparib combined with either MRE11 inhibition or CHD4 depletion. Interestingly, our data revealed that the RF asymmetry observed in these cells upon treatments with olaparib was completely rescued upon MRE11 inhibition

or depletion of CHD4 (Figure 5E). However, MRE11 inhibition or CHD4 depletion did not result in an increase in RF speed in KB1P.R$^{(nucLIG3)}$ cells exposed to olaparib as observed in KB1P.R cells, suggesting that the increase in RF speed is uncoupled from MRE11-mediated ssDNA gap exposure and from PARPi sensitivity (Figures S6I and S6J).

We next tested whether the increase in post-replicative ssDNA gaps upon LIG3 depletion resulted in increased genomic instability. We analyzed chromosomal aberrations in metaphase spreads of KB1P.S+hB1, KB1P.S, KB1P.R, and KB1P.R$^{(nucLIG3)}$ cells after treatment with olaparib for 2 h. As expected, olaparib treatment resulted in increased numbers of chromosomal aberrations in KB1P.S cells but not in KB1P.S+hB1 and KB1P.R (Bunting et al., 2010) (Figures 5F and S7K). Interestingly, KB1P.R$^{(nucLIG3)}$ cells showed a surge in chromosomal aberrations compared with KB1P.R cells (Figures 5F and 5G). Interestingly, the aberrations in PARPi-treated KB1P.R$^{(nucLIG3)}$ cells consisted mainly of chromosome and chromatid breaks, whereas PARPi-treated KB1P.S cells showed more radials (Figure 5G). siRNA-mediated depletion of LIG3 further enhanced chromosomal aberrations in KB1P.S cells (Figure S6K). Of note, inhibition of MRE11 with mirin or siRNA-mediated depletion of CHD4 suppressed PARPi-induced genomic instability in KB1P.R$^{(nucLIG3)}$ cells, indicating that PARPi-induced genomic instability in these cells is mediated by MRE11-dependent ssDNA gap exposure (Figures 5F, 5G, and S6L). As expected, treatment with mirin or depletion of CHD4 did not rescued chromosomal aberrations in parental KB1P.S cells (Figures 5F and 5G). Importantly, loss of LIG3 did not result in an increase in immediate DSBs following olaparib treatment, as assessed by pulsed-field gel electrophoresis (PFGE) of genomic DNA from KB1P.S+hB1, KB1P.S and KB1P.R cells and by immunofluorescence analysis of γ-H2AX foci in K.P, KB1P.S, and KB1P.R cells (Figures S7A and S7B). Altogether, these data indicate that the increase in genomic instability induced by loss of nuclear LIG3 in BRCA1/53BP1 double-deficient cells exposed to PARPi is caused by post-replicative ssDNA gaps.

LIG3 depletion increases *in vivo* efficacy of PARPi

Our previous results established that LIG3 is a modulator of PARPi response *in vitro*. To test whether our results could be recapitulated *in vivo*, we performed shRNA-mediated depletion of LIG3 in PARPi-naive KB1P4.N1 organoids (BRCA1 deficient) and PARPi-resistant KB1P4.R1 organoids (BRCA1/53BP1 double deficient) (Figures 6A and S1A). The modified organoid lines were transplanted into the mammary fat pad of syngeneic wild-type mice. Upon tumor outgrowth, mice were treated with olaparib or vehicle for 28 consecutive days, and mice were sacrificed when tumors progressed to a volume of 1,500 mm³. LIG3 depletion did not affect tumor growth, and all cohorts of vehicle-treated mice showed comparable survival (Figures 6B and 6C). In contrast, LIG3 depletion significantly enhanced the anticancer efficacy of olaparib, resulting in increased survival of olaparib-treated mice bearing KB1P4.N1+shLIG3 tumors, compared with olaparib-treated mice with KB1P4.N1+shscr tumors (Figure 6B). Importantly, LIG3 depletion also resensitized the PARPi-resistant KB1P4.R1 tumors to olaparib. Whereas olaparib-treated and vehicle-treated mice with KB1P4.R1 tumors showed comparable survival, olaparib treatment significantly prolonged the survival of mice bearing KB1P4.R1+shLIG3 tumors (Figure 6C). Together, these data show that LIG3 also modulates PARPi response *in vivo*.

Increased LIG3 expression in triple-negative breast and serous ovarian cancers

To assess the clinical relevance of LIG3, we determined LIG3 expression in sections of treatment-naive tumors from a cohort of 86 women with triple-negative breast cancer (TNBC) (Gogola et al., 2018) and 51 women with high-grade serous ovarian carcinoma (Moudry et al., 2016), two clinically relevant groups of patient eligible for PARPi treatment. Immunohistochemistry (IHC) analysis revealed that although LIG3 protein was expressed at normal levels in a majority of tumor cells in the biopsies, a substantial proportion of samples contained areas displaying aberrant expression of LIG3. Of the 87 TNBC cases analyzed, 32 (37.2%) and 17 (19.8%) biopsies showed LIG3 overexpression in areas corresponding to >10% and >20% of the tumor, respectively (Figure 6D). Similarly, 26 (51%) and 7 (13.7%) of the 51 ovarian cancer cases showed LIG3 overexpression in areas corresponding to >10% and >20% of the tumor, respectively (Figure 6E). Conversely, LIG3-negative areas were observed in a small proportion of biopsies, with 2 (2.3%) and 1 (1.2%) of the 86 TNBC cases and 2 (3.9%) and 4 (7.8%) of the 51 ovarian cancers displaying loss of LIG3 in areas corresponding to >10% and >20% of the tumor, respectively (Figures 6D and 6E). These observations reveal that LIG3 expression is heterogeneous within and across TNBC and serous ovarian cancers, which might result in selective expansion of LIG3 overexpressing clones during PARPi treatment and thereby contribute to intratumoral and inter-patient differences in response to PARPi therapy.

DISCUSSION

Molecular alterations that render cells resistant to targeted therapies may also cause synthetic dependencies, which can be exploited to design rational combination therapies. However, the pathways that can be targeted to exploit these vulnerabilities are poorly understood. In this study, we used shRNA dropout screens to identify synthetic dependencies of BRCA1-deficient cells that acquired resistance to PARPi treatment by restoration of HR due to loss 53BP1. We have identified LIG3 as a critical suppressor of PARPi toxicity in BRCA1/53BP1 double-deficient cells. Loss of LIG3 also enhances PARPi sensitivity of BRCA1-deficient cells with intact 53BP1, indicating that the role of LIG3 in BRCA1-deficient cells is independent of their 53BP1 status.

In this study, we show that the increase in sensitivity to PARPi observed upon LIG3 loss in BRCA1/53BP1 double-deficient cells results from an increase in post-replicative MRE11-dependent ssDNA gaps. This is in line with the notion that PARPi treatment results in accumulation of post-replicative ssDNA gaps and that exposure to these lesions is a key determinant of PARPi response (Cong et al., 2021; Quinet et al., 2020). Moreover, our data show that exposure to post-replicative ssDNA gaps underlies PARPi cytotoxicity in both HR-deficient and HR-restored cells, indicating that LIG3-mediated PARPi resistance in BRCA1/53BP1 double-deficient cells is an HR-independent mechanism. Together, these data indicate that BRCA1/53BP1 double-deficient cells rely on LIG3 for suppression of PARPi-induced gaps, rendering LIG3 as a synthetic dependency of these cells. LIG3 depletion also increased sensitivity to PARPi in BRCA1/REV7 double-deficient cells, suggesting this synthetic dependency is common to BRCA1-deficient tumor cells that acquired PARPi resistance due to loss of end-protection.

We show that PARPi-induced ssDNA gaps in BRCA1-deficient cells are not substrates for MRE11-mediated degradation, indicating that PARPi-induced ssDNA gaps observed in LIG3-depleted BRCA1/53BP1 double-deficient cells are distinct from the gaps in BRCA1-deficient cells. Together, these data suggest existence of two different mechanisms of gap suppression in BRCA1-deficient cells, one dependent on loss of 53BP1 and another which is LIG3 dependent. In PARPi-sensitive BRCA1-deficient cells, 53BP1 drives the formation of post-replicative ssDNA gaps upon PARPi treatment. Loss of LIG3 in these cells further enhances accumulation of PARPi-induced ssDNA gaps. On the other hand, PARPi-resistant BRCA1/53BP1 double-deficient cells are competent for HR and thus lack 53BP1-mediated gap formation, hence PARPi-induced ssDNA gaps only occur upon loss of LIG3 (Figure 7).

53BP1-mediated gap induction in BRCA1-deficient cells exposed to PARPi may result from loss of recombinatorial gap repair (Branzei and Szakal, 2016) and/or defective Okazaki fragment processing (OFP) due to loss of the PARP1-XRCC1-LIG3 backup pathway (Arakawa and Iliakis, 2015; Cong et al., 2021; Hanzlikova et al., 2018). Cong et al. (2021) have also suggested that PARPi resistance in BRCA1/53BP1 double-deficient cells is caused by restoration of the OFP backup pathway, evidenced by higher levels of chromatin-bound XRCC1 and LIG3 in these cells. Although we find that the LIG3 BRCT domain, required for interaction with XRCC1, is critical for PARPi resistance in BRCA1/53BP1 double-deficient cells, we also find that PARPi-induced ssDNA gap formation in LIG3-depleted BRCA1/53BP1 double-deficient cells is fully rescued by MRE11 inhibition, indicating that LIG3 depletion in these cells does not impair OFP. Moreover, PARPi-induced ssDNA gaps in LIG3-depleted BRCA1/53BP1 double-deficient cells occur in both the newly replicated strands. Together, these data indicate that LIG3 is also involved in a separate, OFP-independent pathway of gap suppression.

Mechanistically, the LIG3-dependent gap suppression pathway might require repriming activities mediated by Polα, PRIMPOL, or another unknown primase for bypass of lesions such as PARPi-trapped PARP1 in BRCA1-deficient cells (Fumasoni et al., 2015; García-Gómez et al., 2013; Piberger et al., 2020; Quinet et al., 2020). These repriming activities could result in small gaps that require LIG3 to be filled. Loss of LIG3 in BRCA1-deficient and BRCA1/53BP1 double-deficient cells could thus result in the exposure of small ssDNA regions, which would be a substrate for unscheduled MRE11-mediated processing. Subsequent processing of the small ssDNA regions could result in accumulation of longer stretches of post-replicative ssDNA, ultimately resulting in RF stalling, genomic instability, and cell death (Figure 7).

PARP1 has recently been implicated in restraining RF speed in cells (Maya-Mendoza et al., 2018). We indeed observe an increase of RF speed in BRCA1-deficient cells treated with low doses of PARPi. Importantly, the increase in speed was specific to cells deficient for BRCA1, contrasting with previous studies in which PARP inhibition increased RF speed in BRCA1-proficient cells (Maya-Mendoza et al., 2018), possibly reflecting the use of higher olaparib concentrations and longer periods of exposure to PARPi in the latter study. In addition, we observe that PARPi treatment induces faster RFs in PARPi-sensitive BRCA1-deficient cells as well as in PARPi-resistant BRCA/53BP1 double-deficient cells. Moreover, loss of LIG3 induces PARPi (hyper) sensitivity but suppresses PARPi-induced

increase in RF speed in both BRCA1-deficient and BRCA1/53BP1 double-deficient cells. Together, these data show that PARPi-induced increase in RF speed in BRCA1-deficient cells is HR independent and not causally related to PARPi sensitivity, in line with previous findings from Cong et al. (2021).

Our findings might have therapeutic implications, as LIG3 depletion also increases the efficacy of PARPi *in vivo*, resulting in prolonged survival of mice bearing PARPi-sensitive BRCA1-deficient or PARPi-resistant BRCA1/53BP1 double-deficient mammary tumors. Furthermore, we find LIG3 to be overexpressed in a portion of TNBC and serous ovarian cancers, further suggesting that LIG3 could possibly be targeted in these cancers. Pharmacological inhibition of LIG3 might therefore be a potential strategy to combat resistance to PARPi. Taken together, our findings establish loss of LIG3 as a potent enhancer of PARPi synthetic lethality in BRCA1-deficient tumors, irrespective of their HR status, and provide insights into the role of LIG3 in restraining replication stress and genome instability induced by BRCA1 loss.

Limitations of this study

In this study we show that resistance to PARPi in BRCA1/53BP1 double-deficient cells is mediated by nuclear LIG3. As previously mentioned, mitochondrial LIG3 is essential for cellular viability and complete deletion of *Lig3* results in cellular death and early embryonic lethality in mice, whereas nuclear LIG3 is dispensable for cell viability (Simsek et al., 2011). In this study we have engineered BRCA1/53BP1 double-deficient mouse mammary tumor cells that express only mitochondrial *Lig3*, ensuring complete loss of nuclear *Lig3* expression. However, experiments testing olaparib sensitivity in other cell models were carried out using RNAi-mediated depletion, which can result in downregulation of both isoforms. Thus, we cannot exclude the possibility that the observed effects are partially due to depletion of mitochondrial LIG3. In addition, our data indicate that loss of LIG3 has a more profound effect on PARPi sensitivity of BRCA1-deficient cells compared with BRCA2-deficient cells. However, it was not possible to compare the effects of LIG3 loss on PARPi sensitivity in isogenic cell lines deficient for either BRCA1 or BRCA2. Therefore, we cannot rule out that the observed differences were due in part to intercellular variability.

Although our findings might have clinical implications, datasets for large numbers of patients with *BRCA1*-mutated tumors who received PARPi treatment are not (yet) available. Finally, although our data suggest LIG3 as potential therapeutic target, small-molecule inhibitors of LIG3 could target both nuclear and mitochondrial isoforms and might therefore result in undesirable toxicity.

STAR★METHODS

Detailed methods are provided in the online version of this paper and include the following:

RESOURCE AVAILABILITY

Lead contact—Further information and requests for resources and reagents should be directed to and will be fulfilled by the Lead Contact, Jos Jonkers (j.jonkers@nki.nl).

Materials availability—Materials associated with this study are available upon request from the lead contact.

Data and code availability

- Original western blot, agarose gel and microscopy images have been deposited at Mendeley and are publicly available as of the date of publication. The DOI is listed in the key resources table. Microscopy data reported in this paper is available from the lead contact upon request.

- This paper does not report original code

- Any additional information required to reanalyze the data reported in this paper is available from the lead contact upon request.

EXPERIMENTAL MODEL AND SUBJECT DETAILS

Cell lines and cell culture—KP (Evers et al., 2008), KB1P.S, KB1P.R (Jaspers et al., 2013) and KB1P.S+hB1 (Barazas et al., 2019) have been previously described. LIG3 nuclear mutants, KB1P.R-B1, KB1P.R-A3 and KB1P.R-F5, have been generated in this study. All these cell lines were cultured in in DMEM/F12+GlutaMAX (GIBCO) containing 5 μg/ml Insulin (Sigma, #I0516), 5 ng/ml cholera toxin (Sigma, #C8052), 5 ng/ml murine epidermal growth-factor (EGF, Sigma, #E4127), 10% FBS and 50 units/ml penicillin-streptomycin (GIBCO) and were cultured under low oxygen conditions (3% O2, 5% CO_2 at 37°C). Mouse ES cells with a selectable conditional *Brca1* deletion ($R26Cre^{ERT2/wt};Brca1^{SCo/-}$) have been previously described (Bouwman et al., 2010). Additional knockout of *Trp53, Trp53bp1* and *Parp1* has been generated in this study. These cells were cultured on gelatin-coated plates in 60% buffalo red liver (BRL) cell conditioned medium, 0.1 mM β-mercaptoethanol (Merck) and 10^3 U/ml ESGRO LIF (Millipore) and 50 units/ml penicillin-streptomycin (GIBCO) under normal oxygen conditions (21% O2, 5% CO_2, 37°C). SUM149PT (RRID: CVCL_3422) cells were grown in RPMI1640 (GIBCO) medium supplied with 10% fetal calf serum and 50 units/ml penicillin-streptomycin (GIBCO). RPE1-hTERT and DLD-1 cell lines were grown in DMEM+GlutaMAX (GIBCO) supplemented with 10% FBS and 50 units/ml penicillin-streptomycin (GIBCO). RPE1-P, RPE1-B1P.S and RPE1-B1P.R cells were generated by Noordermeer et al., 2018. HEK293FT (RRID: CVCL_6911) cells were cultured in IMDM+GlutaMAX-I (GIBCO) supplemented with 10% FBS and 50 units/ml penicillin-streptomycin (GIBCO). SUM149PT and DLD1 cell lines were cultured under normal oxygen conditions (21% O2, 5% CO_2, 37°C). RPE1 cell lines were cultured under low oxygen conditions (3% O2, 5% CO_2 at 37°C).

Tumor-derived organoids—All lines have been described before (Duarte et al., 2018). ORG-KB1P.S and ORG-KB1P.R tumor organoids were derived from a PARPi-naive and PARPi-resistant $K14cre;Brca1^{F/F};Trp53^{F/F}$ (KB1P) mouse mammary tumor, respectively. The ORG-KP tumor organoid line was derived from a $K14cre;Trp53^{F/F};Abcb1a^{-/-};Abcb1b^{-/-}$ (KPM) mouse mammary tumor. Cultures were embedded in Culturex Reduced Growth Factor Basement Membrane Extract Type 2 (BME, Trevigen; 40 mL BME:growth media 1:1 drop in a single well of 24-well plate) and grown in Advanced DMEM/F12 (GIBCO) supplemented with 1M HEPES (GIBCO), GlutaMAX

(GIBCO), 50 units/ml penicillin-streptomycin (GIBCO), B27 (GIBCO), 125 mM N-acetyl-L-cysteine (Sigma) and 50 ng/ml murine epidermal growth factor (Sigma). Organoids were cultured under standard conditions (37°C, 5% CO_2) and regularly tested for mycoplasma contamination.

Mice—All animal experiments were approved by the Animal Ethics Committee of the Netherlands Cancer Institute (Amsterdam, the Netherlands) and performed in accordance with the Dutch Act on Animal Experimentation (November 2014). Organoid transplantation experiments were performed in syngeneic, wild-type F1 FVB (FVB/NRj) females, at the age of 6 weeks. Parental FVB animals were purchased from Janvier Labs. Animals were assigned randomly to the treatment groups and the treatments were supported by animal technicians who were blinded regarding the hypothesis of the treatment outcome.

Human samples of TNBC and ovarian serous carcinomas—Samples were previously described in (Gogola et al., 2018). Retrospective Triple Negative Breast Cancer (TNBCs) biopsies from 86 clinical high-risk patients (high-risk definition according to the Danish Breast Cooperative Group (https://www.dbcg.dk/ accessed 22.10.2009) that underwent mastectomy between 2003 and 2015 were selected and classified as being triple negative according to the criteria set in the ASCO/CAP guidelines (ER < 1%, PR < 1%, HER2 0, 1+ or 2+ but FISH/CISH negative). The patients presented a unifocal tumor of an estimated size of more than 20 mm. None of the patients had previous surgery to the breast and did not receive preoperative treatment. This study was conducted in compliance with the Helsinki II Declaration and written informed consent was obtained from all participants and approved by the Copenhagen and Frederiksberg regional division of the Danish National Committee on Biomedical Research Ethics (KF 01-069/03). Paraffin-embedded material from the cohort of ovarian tumors was collected at the Department of Pathology, University Hospital, Las Palmas, Gran Canaria, Spain, from surgical operations performed in the period 1995–2005. For the purpose of the present study, only samples from serous ovarian carcinoma (the type approved for treatment by PARP inhibitors) were used from a larger cohort that was reported previously (Moudry et al., 2016), and included also other histological types of ovarian tumors. The use of long-term stored tissue samples in this study was in accordance with the Spanish codes of conduct (Ley de Investigación Biomédica) and was approved by the review board of the participating institution. Patients were informed that samples may be used for research purposes under the premise of anonymity.

METHOD DETAILS

Functional genetic screens—The DDR shRNA library was stably introduced into *Brca1*^{−/−};*Trp53*^{−/−};*Trp53bp1*^{−/−} mESCs and in KB1P4.R1 by lentiviral transduction using a multiplicity of transduction (MOI) of 1, in order to ensure that each cell only gets incorporated with one only shRNA. mES cells and organoids were selected with puromycin, 3 μg/ml, for 3 days and then seeded in the presence of PARPi (mES cells, 25nM olaparib; organoids, 50nM), left untreated or pelleted for the genomic DNA isolation (T0). The total number of cells used in a single screen was calculated as following: library complexity × coverage (5000x in mESc, 1000x in organoids). Cells were kept in culture for 3 weeks and passaged every 5 days (and seeded in single cells) while keeping the coverage at every

passage. mES cells were seeded at a density of 2,500 cells per 15 cm dish and organoids at a density of 50,000 cells/well, 24-well format. Screens were done in triplicate for each condition. In the end of the screen, cells were pooled and genomic DNA was extracted (QIAmp DNA Mini Kit, QIAGEN). shRNA sequences were retrieved by a two-step PCR amplification, as described before (Xu et al., 2015). To maintain screening coverage, the amount of genomic DNA used as an input for the first PCR reaction was taken into account (6 μg of genomic DNA per 10^6 genomes, 1 μg/PCR reaction). Resulting PCR products were purified using MiniElute PCR Purification Kit (QIAGEN) and submitted for Illumina sequencing. Sequence alignment and dropout analysis was carried out using the algorithms MAGeCK (Li et al., 2014) (FDR 0.1) and DESeq2 (Love et al., 2014) (FDR 0.05, log2Fc −2, baseMean > = 100, at least 3 hit shRNA in the depletion direction and none in the opposite direction). In order to reduce the noise level, we filtered out sgRNAs with low counts in the T0 sample: mESc, sum of the three T0 samples > = 10, organoids, mean over the three T0 samples > = 50. Gene ranking is generated automatically with MaGECK algorithm. To generate gene ranking based on DESeq2 algorithm, we calculated per gene the number of hit shRNAs and the mean of the log2FoldChange over those shRNAs. We then ranked the genes based on these two metrics.

Constructs—A collection of 1,976 lentiviral hairpins targeting 391 DDR-related mouse genes (pLKO.1; DDR library) was derived from the Sigma Mission library (TRCMm1.0) as described before (Xu et al., 2015). Individual hairpin constructs used in the validation studies were selected from the TRC library: mouse LIG3 shRNA #1: TRCN0000070978, mouse LIG3 shRNA #2: TRCN0000070982, mouse REV7 shRNA: TRCN0000006570, human LIG3 shRNA #1: TRCN0000048498, human LIG3 shRNA #2: TRCN0000300259. For CRISPR/Cas9-mediated genome editing of *Parp1*, a sgRNAs was cloned into plentiGuide-Puro (lentiviral) as described previously (Sanjana et al., 2014). For the LIG3 overexpression constructs, human α-LIG3 wild-type, human α-LIG3 carrying a mutation in the PARP-like ZnF domain (R31L), and human α-LIG3 with a C-terminal 774–922 truncation which includes the BRCT domain were cloned into PCW57.1 plasmid. All constructs were verified by Sanger sequencing.

Lentiviral transductions—Lentiviral stocks, pseudotyped with the VSV-G envelope, were generated by transient transfection of HEK293FT cells, as described before (Follenzi et al., 2000). Production of integration-deficient lentivirus (IDLV) stocks was carried out in a similar fashion, with the exception that the packaging plasmid contains a point mutation in the integrase gene (psPAX2, gift from Bastian Evers). Lentiviral titers were determined using the qPCR Lentivirus Titration Kit (Applied Biological Materials), following the manufacturer's instructions. For all experiments the amount of lentiviral supernatant used was calculated to achieve an MOI of 50, except for the transduction of the lentiviral library for which a MOI of 1 was used, as described above. Cells were incubated with lentiviral supernatants overnight in the presence of polybrene (8 μg/ml). Tumor-derived organoids were transduced according to a previously established protocol (Duarte et al., 2018). Antibiotic selection was initiated right after transduction for cells, 24h after transduction in organoids, and was carried out for 3 consecutive days.

Genome editing—For CRISPR/Cas9-mediated genome editing of *Trp53* in mESCs, *R26Cre^{ERT2/wt};Brca1^{SCo/−}* cells (Bouwman et al., 2010) were transiently transfected with a modified a pX330-U6-Chimeric-BB-CBh-hSpCas9 plasmid containing a puromycin resistance marker (Cong et al., 2013; Drost et al., 2016) in which a sgRNA targeting *Trp53* was cloned. Knockout clones were selected under puromycin for 3 days and tested by TIDE and western blot.

For CRISPR/Cas9-mediated genome editing of *Trp53bp1* in mESCs, Cas9-expressing *R26Cre^{ERT2/Cas9};Brca1^{SCo/−};Trp53^{−/−} cells* (Barazas et al., 2018) were incubated with lentiviral supernatants of pLentiGuide-Puro cloned with a sgRNA targeting *Trp53bp1.* After selection with puromycin for 3 days, surviving cells were subcloned and tested by TIDE and western blot.

For CRISPR/Cas9-mediated genome editing of *Parp1, the* Cas9-expressing *R26Cre^{ERT2/Cas9}; Brca1^{−/−};Trp53^{−/−};Trp53bp1^{−/−}* mESCs were incubated with lentiviral supernatants of pLentiGuide-Puro cloned with a sgRNA targeting *Parp1.* After selection with puromycin for 3 days, surviving cells were subcloned and tested by TIDE and western blot.

For the disruption of the starting codon encoding for nuclear LIG3, the desired mutation (ATG > CTC) was introduced in KB1P.R mouse tumor cells according to the Alt-R CRISPR-Cas9 System of IDT (Yoshimi et al., 2016). Briefly, the crRNA targeting sequence and the homology template, a 120bp ssODN, were designed using CRISPR design tools of Benchling. While the sgRNA was designed to target the nuclear ATG, the homology template contains an ATG > CTC mutation, encoding a leucine instead of the original methionine. 10 μl tracrRNA (100 μM) and 10 μl crRNA (100 μM) were annealed in 80 μL nuclease free duplex buffer (IDT#11-05-01-03) to form a 10μM gRNA solution. The ssODN template was also annealed to form a 10μM solution. 6 μL of 10 μM sgRNA, 6 μl of 10 μM Cas9 protein, and 6 μl of 10 μM ssODN (Ultramer IDT) were mixed in optiMEM (GIBCO), to final volume of 125 μl and incubated for 5 min at RT (Mix 1). Then, 3μl of Lipofectamine RNAiMAX (Invitrogen) were mixed with 122 μl with optiMEM (Mix 2). Mix 1 and mix 2 were mixed together and incubated at RT for 20 min. During these 20 min, 150.000 cells were trypsinized and collected in 750 μl of medium. The 250 μl Mix was then added to the cells in a 12-well for reverse transfection. Next day cells were expanded and 3 days after transfection the cells were harvested for analysis of the genomic DNA.

To assess modification rate, genomic DNA was extracted (Puregene Core Kit A, QIAGEN) and 100 ng was used as an input for the PCR amplification of the targeted sequence. PCR reaction was performed with Thermo Scientific Phusion High-Fidelity PCR Master Mix (Thermo Scientific), according to manufacturer's instructions (3-step protocol: annealing - 60C for 5 s, extension time 30 s) and using primers listed in Table S2. Resulting PCR products served as a template for the BigDye Terminator v3.1 reaction (Thermo Fisher). BigDye PCR reactions were performed with the same forward primers as in the preceding PCR reactions (no reverse primer used) and according to the BigDye manufacturer's protocol. For knockout, allele composition was determined with the TIDE analysis (Brinkman et al., 2014) by comparing sequences from modified and parental (transduced

with non-targeting sgRNAs) cells. For knock-in, allele composition was determined with the TIDER analysis (Brinkman et al., 2018) by comparing sequences from modified and parental cells (transduced with non-targeting sgRNAs), and reference template. The later was generated with a simple two-step PCR protocol, with two complementary primers designed to carry the designed mutations as present in the donor template (Brinkman et al., 2018).

siRNA and transfections—Non-targeting siRNA and siRNA against mouse and human LIG3 were transfected into the cells using Lipofectamine RNAiMAX (Invitrogen) according to the manufacturer's instructions. All experiments were carried out between 48 and 72hr post-transfection.

Long-term clonogenic assays—Long-term clonogenic assays were always performed in 6-well plates, with exception of organoids which were cultured in 24-well plated as described before, and to DLD-1 cells which was performed in a 12-well plate. Cells were seeded at low density to avoid contact inhibition between the clones (KB1P.S: 5,000 cells/well; KB1P.R: 2,500 cells/well; ORG-KB1P.S and ORG-KB1P.R: 50.000 cells/well; ES-B1P.R and ES-P.R: 3,000 cells/well; ES-B1P.S and ES-P: 5,000 cells/well; SUM149PT: 5,000 cells/well; RPE1-P: 3,000 cells/well, RPE1-B1P.S and RPE1-B1P.R: 5,000 cells/well; DLD-1: 3,500 cells/well; DLD-1 BRCA2 KO cells: 5,000) and cultured for 10–15 days. Media was refreshed once a week. For the quantification, cells were incubated with Cell-Titer Blue (Promega) reagent and later fixed with 4% formaldehyde and stained with 0.1% crystal violet. Drug treatments: cells were grown in the continuous presence of PARPi (olaparib, talazoparib or veliparib) at the indicated concentrations. mESCs with a selectable conditional *Brca1* deletion were treated with 0.5μM 4OHT for 3 days right before the start of the clonogenic assay, when indicated. PAR-Pis were reconstituted in DMSO (10 mM) and 4OHT in EtOH (2.5 mM). Expression of human LIG3 constructs was induced with treatment with 2 μM Doxycycline for two days prior to the start of the assay and at the start of the assay.

Proliferation assay—Cell were imaged every 4h using IncuCyte ®, for 1 week duration. Cells were seeded at low density and grown under normal oxygen conditions (21% O_2, 5% CO_2, 37°C). Data was analyzed using IncuCyte ZOOM 2018A software.

RT-qPCR—In order to determine gene expression levels, RNA was extracted from cultured cells using ISOLATE II RNA Mini Kit (Bioline) and used as a template to generate cDNA with Tetro cDNA Synthesis Kit (Bioline). Quantitative RT-PCR was performed using SensiMix SYBR Low-ROX Kit (Bioline; annealing temperature −60°C) in a Lightcycler 480 384-well plate (Roche), and analyzed using Lightcycler 480 Software v1.5 (Roche). Mouse *Rps20* and human *HPRT* were used as house-keeping genes. The primer sequences used in this study are listed in Table S2.

Western blot—Cells were trypsinized and then lysed in lysis buffer (20 mM Tris pH 8.0, 300 mM NaCl, 2% NP40, 20% glycerol, 10 mM EDTA, protease inhibitors (complete Mini EDTA-free, Roche, 100x stock)), for 20 min. For PAR detection in PARP1 knockout mES cells, 10μM PARGi was added to the lysis buffer, when indicated. For P53 detection,

cells were irradiated at $15 \times 100\ \mu J/cm^2$. The protein concentration was determined using Pierce BCA Protein Assay Kit (Thermo Scientific). SDS-Page was carried out with the Invitrogen NuPAGE SDS-PAGE Gel System (Thermo Fisher; for LIG3: 2%–8% Tris-acetate gels were used, buffer Tris-Acetate; for all other proteins: 4–12% Bis-Tris gels were used, buffer: MOPS; input: 40μg protein), according to the manufacturer's protocol. Next, proteins were electrophoretically transferred to a nitrocellulose membrane (Biorad). Before blocking, membranes were stained with Ponceau S, followed by blocking in 5% (w/v) milk in TBS-T for 1hr at RT. Membranes were incubated with primary antibody 4hrs at RT in 1% (w/v) milk in TBS-T (rabbit anti-PARP1, 1:1000; rabbit anti-H3, 1:5000; mouse anti-lig3, 1:500; rabbit anti-lig3, 1:1000; rabbit anti-tubulin, 1:1000; anti-PAR, 1:1000; mouse anti-P53, 1:1000). Horseradish peroxidase (HRP)-con-jugated secondary antibody incubation was performed for 1 hr at RT (anti-mouse or anti-rabbit HRP 1:2000) in 1% (w/v) milk in TBS-T. Signals were visualized by ECL (Pierce ECL Western Blotting Substrate, Thermo Scientific).

Cytotoxicity assays—Cytotoxicity assays were carried in 96-well plates, for 3 days. Olaparib and POLθ inhibitor ART558 were used at the indicated concentrations. Olaparib was used at concentrations that wouldn't lead to lethality of LIG3-depleted cells when used as single agent in order to allow a window to detect the effect of POLθ inhibition. KB1P.R and KB1P.R A3 cells were seeded at high density, 2.000 cells/well. For the quantification, cells were incubated with Cell-Titer Blue (Promega) reagent. The expected drug combination responses were calculated based on Bliss reference model using SynergyFinder (Ianevski et al., 2020).

Proximity ligation assay (PLA)—Protocol was carried out as mentioned previously (Mukherjee et al., 2019). On coverslips, cells were grown to a confluence of 60%–70%. On the day of the experiment, cells were incubated with PARGi (10μM) for a total of 30 minutes or 0.5 μM olaparib for 2hr and the final 10 minutes cells were incubated with EdU (20 μM) during PARGi incubation to visualize S-phase cells. After EdU labeling cells were gently washed two times with PBS and fixed with 4% paraformaldehyde for 15 min at RT. PFA was discarded after fixation and slides were washed with cold PBS for 8 minutes each three times. Cells were next permeabilized by incubating the coverslips in PBS containing 0.5% Triton-X for 15 min at RT and subsequently washed in PBS twice for 5 min each. Freshly prepared click reaction mix (2mM of copper sulfate, 10 μM of biotin-azide and 100 mM of sodium ascorbate were added to PBS in that order and mixed well) was applied to the slides (30 μl/slide) in a humid chamber and incubated for 1 hr at RT. Slides were washed with PBS for 5 min after the click reaction and placed back in the humid chamber and blocked at room temperature for 1 hr with a blocking buffer (10% goat serum and 0.1%Triton X-100 in PBS). In combination with anti-biotin (1:1000), rabbit anti-LIG3 (1:150, Sigma-Aldrich, #HPA006723) primary antibody was diluted in a blocking solution, dispensed to slides (30 μl/slide) and incubated in a humid chamber at 4°C overnight. Slides were washed with wash buffer A (0.01 M Tris-HCl, 0.15 M NaCl, and 0.05% Tween-20, pH 7.4) for 5 min each after overnight incubation. Duolink *In Situ* PLA probes, the anti-mouse plus and anti-rabbit minus were diluted 1:5 in the blocking solution (10% goat serum and 0.1% Triton X-100 in PBS), dispensed to slides (30 μl/well) and incubated at 37°C for 1 hr. Slides were washed

three times with buffer-A, 5 min each. The ligation mix was prepared by diluting Duolink ligation stock (1:5) and ligase (1:40) in high purity water and was applied to slides (30 μl/well) and incubated at 37°C for 30 min. Slides were washed with buffer-A twice for 2 min each. Amplification mix was prepared by diluting Duolink amplification stock (1:5) and rolling circle polymerase (1:80) in high-purity water and applied to slides (30 μL/well) and incubated for 100 min at 37°C in a humid chamber. Slides were washed with wash buffer-B solution (0.2 M Tris and 0.1 M NaCl) three times for 10 min each and one time in 0.01X diluted wash buffer-B solution for 1 min. Coverslips were incubated with DAPI for 5 min and mounted with ProLong Gold antifade reagent (Invitrogen) and imaged using confocal and analyzed using ImageJ software 64.

Immunofluorescence

RAD51 IRIF: Cells were seeded on Millicell EZ slides (#PEZGS0816, Millipore) 24 hr prior the assay to achieve ~90% confluency. Cells were then irradiated using the Gammacell 40 Extractor (Best Theratronics Ltd.) at the dose of 10 Gy and allowed to recover for 3 hr. Cells washed with PBS++ (PBS solution containing 1 mM CaCl2 and 0.5 mM MgCl2) and pre-extracted with 0.5% (v/v) Triton X-100 in PBS++ for 5 min. Next, cells were washed with PBS++ and fixed with 2% (v/v) paraformaldehyde solution in PBS for 20 min. Next, cells were permeabilized with ice-cold methanol/acetone solution (1:1) for 15 min. To minimize the background, cells were further incubated for 20 min in staining buffer (1% (w/v) BSA, 1% (v/v) FBS, 0.15% (w/v) glycine and 0.1% (v/v) Triton X-100 in PBS). Staining buffer was also used as a solvent for antibodies – primary antibody anti-RAD51, 1:1500, #ab133534, abcam; secondary antibody Alexa Fluor® 658-conjugated, 1:1000, A11011, Invitrogen. Incubation with primary and secondary antibodies was done for 2 hr and 1 hr, respectively. All incubations were performed at room temperature. Samples were mounted with VECTASHIELD Hard Set Mounting Media with DAPI (#H-1500; Vector Laboratories). Images were captured with Leica SP5 (Leica Microsystems) confocal system and analyzed using an in-house developed macro to automatically and objectively evaluate the DNA damage-induced foci (Xu et al., 2015). As a positive and negative control for RAD51 staining, BRCA-proficient KP and BRCA1-deficient KB1P.S cells were used.

LIG3-EdU co-localization: Cells were incubated with 20 μM EdU for 1hr to visualize cells in S-phase. In the last 20 min, 10μM PARGi was added to the medium. Cells washed with PBS and pre-extracted with CSK50 buffer for 7 min (10μM PARGi PDDX-001 was added to pre-extraction buffer). Cells were washed with PBS and fixed with 4% formaldehyde, followed by three washes with PBS and permeabilization with ice-cold methanol/acetone solution (1:1). EdU Click-iT reaction mix was added to each well and incubated at RT for 30 min. Fixed cells were washed three times with staining buffer (5% (v/v) FBS, 5% (w/v) BSA, and 0.05% (v/v) Tween-20 in PBS) and incubated with primary antibody anti-LIG3 (1:150, Sigma-Aldrich, #HPA006723) in staining buffer for 2hr at RT. After three washes in staining buffer, cells were incubated with secondary antibody anti–rabbit Alexa Fluor 488 (1:500, A27034, Invitrogen) in staining buffer, followed by three last washes in staining buffer and one wash in PBS. Samples were mounted with VECTASHIELD Hard Set Mounting Media with DAPI (#H-1500; Vector Laboratories). Images were captured with Leica SP5 (Leica Microsystems) confocal system and analyzed with ImageJ software.

Native BrdU: Cells were labeled with 10 μM BrdU for 48hr. When indicated, cells were incubated with Mirin (25 μM) for the same 48hr. Upon treatment with the final 2hr PARPi inhibitor (0.5 μM), the cells were washed with PBS and pre-extracted by CSK-buffer (PIPES 10mM, NaCl 100mM, Sucrose 300mM, EGTA 250mM, MgCl2 1mM, DTT 1mM and protease inhibitors cocktail) on ice for 5 minutes. Cells were then fixed using 4% formaldehyde (FA) for 15 min at RT, and then permeabilized by 0.5% Triton X-100 in CSK-buffer. Permeabilized cells were then incubated with primary antibody against anti-BrdU antibody (Abcam 6326) at 37°C for 1 hr. Cells were washed and incubated with secondary antibodies (Alexa Fluor 594) for 1h at room temp. After the wash cells were incubated with DAPI (0.1 μg/ml) for 5 minutes. For mouse tumor cells (high content imaging), DAPI and ssDNA signal, Z stack of 6 stacks (1mm/stack) covering at least 75 fields were imaged. Results were analyzed using DAPI channel and filtered with roundness and size of the nucleus. The quantification of pixel intensities (mean, median and sum) for each nucleus was calculated in the DAPI and 594 nm channels. The quantified values obtained were exported to Tibco spotfire software (TIBCO Spotfire ®) for the generation of scatterplots. For human RPE1 cells, images were collected by fluorescence microscopy (Axioplan 2 and Axio Observer, Zeiss) at a constant exposure time in each experiment. Representative images were processed by ImageJ software. Mean intensities of ssDNA in each nucleus were measured with Cell Profiler software version 3.1.5 from Broad Institute.

H2AX foci: Cells were incubated treated for 2hr with PARPi inhibitor (0.5 μM). Cells were then washed with PBS and fixed with 4% formaldehyde, followed by three washes with PBS and permeabilization with ice-cold methanol/acetone solution (1:1). Fixed cells were washed three times with staining buffer (5% (v/v) FBS, 5% (w/v) BSA, and 0.05% (v/v) Tween-20 in PBS) and incubated with primary antibody anti-H2AX (Ser139) (1:1000, Cell Signaling, Cat#2577) in staining buffer for 2hr at RT. After three washes in staining buffer, cells were incubated with secondary antibody anti–rabbit Alexa Fluor 488 (1:500, A27034, Invitrogen) in staining buffer, followed by three last washes in staining buffer and one wash in PBS. Samples were mounted with VECTASHIELD Hard Set Mounting Media with DAPI (#H-1500; Vector Laboratories). Images were captured with Leica SP5 (Leica Microsystems) confocal system and analyzed with ImageJ software.

DNA fiber assay

Mouse tumor cells: DNA fiber analysis was conducted in accordance with the previously described protocol (Ray Chaudhuri et al., 2012). Briefly, cells were transfected for 48 hours followed by treatment with olaparib (0.5μM), or left untreated, for the final two hours. Cells were sequentially pulse-labeled with nucleotide analogs, 30μM CldU (c6891, Sigma-Aldrich) and 250μM IdU (I0050000, European Pharmacopoeia) for 20 min during the incubation of olaparib. After double labeling, cells were washed with PBS, harvested and resuspended in ice cold PBS to the final concentration 2.5×10^5 cells per ml. Labeled cells were mixed with unlabeled cells at 1:1 (v/v), and 2.5 μl of cell suspension was spotted at the end of the microscope slide. 8 μl of lysis buffer (200mM Tris-HCl, pH 7.5, 50mM EDTA, and 0.5% (w/v) SDS) was applied on the top of the cell suspension, then mixed by gently stirring with the pipette tip and incubated for 8 min. Following cell lysis, slides were tilted to 15–45° to allow the DNA fibers spreading along the slide, air-dried, fixed

in 3:1 methanol/acetic acid overnight at 4°C. Subsequently, fibers were denatured with 2.5 M HCl for 1 hr. After denaturation, slides were washed with PBS and blocked in blocking solution (0.2% Tween 20 in 1% BSA/PBS) for 40 min. After blocking, primary antibody solutions are applied, anti-BrdU antibody recognizing CldU (1:500, ab6326; Abcam) and IdU (1:100, B44, 347580; BD) for 2 hours in the dark at RT followed by 1h incubation with secondary antibodies: anti–mouse Alexa Fluor 488 (1:300, A11001, Invitrogen) and anti–rat Cy3 (1:150, 712-166-153, Jackson Immuno-Research Laboratories, Inc.). Finally, slides are washed with PBS and subsequently mounting medium is spotted and coverslips are applied by gently pressing down. Slides were sealed with nail polish and air-dried. Fibers were visualized and imaged by Carl Zeiis Axio Imager D2 microscope using 63X Plan Apo1.4 NA oil immersion objective. Data analysis was carried out with ImageJ software64.

RPE1-hTERT cells: These assays were performed as previously described (Cong et al., 2021; Peng et al., 2018). Briefly, cells were treated for 2 hr with 0.5μM olaparib or left untreated. During the last 40 min, cells were labeled by sequential incorporation of IdU and CldU into nascent DNA strand. Cells were then collected, washed, spotted, and lysed on positively charged microscope slides by 7.5 mL spreading buffer for 8 min at RT. Individual DNA fibers were released and spread by tilting the slides at 45°C. After air-drying, fibers were fixed by 3:1 methanol/acetic acid at RT for 3 min. Fibers were then rehydrated in PBS, denatured with 2.5 M HCl for 30 min, washed with PBS, and blocked with blocking buffer for 1 hr. Next, slides were incubated for 2.5 hr with primary antibodies diluted in blocking buffer (IdU, B44, 347580; BD; CldU, ab6326, Abcam), washed several times in PBS, and then incubated with secondary antibodies in blocking buffer for 1 hr (IdU, goat anti-mouse, Alexa 488; CldU, goat anti-rat, Alexa Fluor 594). After washing and air-drying, slides were mounted with Prolong (Invitrogen, P36930). Finally, fibers were visualized and imaged with Axioplan 2 imaging, Zeiss.

Metaphase spreads and telomere FISH—Metaphase spreads were carried out according to the standard protocol described previously (Mukherjee et al., 2019). Briefly, exponentially growing cells (50%–80% confluence) were treated with 0.5μM olaparib for 2hr or left untreated, and recovered for 6 hr. Post treatment, drug treated medium was washed out and cells were allowed to grow in complete growth medium and exposed with colcemid for 8 h. Metaphase spreads were prepared by conventional methods and check under the microscope before telomere labeling. Metaphase slides in coplin jar containing 2X SSC buffer (Sigma-S6639) were equilibrated at room temperature for 10 minutes. Proteins were digested by incubation of the slides in pre-warmed 0.01M HCl containing pepsin for 1.5 min at 37°C. Slides were washed twice with PBS 5 min each and then one time with 1 M MgCl2 in 1X PBS for 5 min. After washing slides were placed in coplin jar containing 1% formaldehyde and fixed for 10 mins at RT without shaking. Slides were washed with PBS and dehydrated in the ethanol series: 70%, 90% and 100% for 3 minutes each and air-dried. Next, slides were denatured in 70% deionized formamide at 80°C for 1 min 15 s and immediately placed in chilled ethanol series 70%, 90% and 100% for 3 minutes each and allowed slides for air dry. Pre-annealed telomere probes were added to the denatured slides and allowed for hybridization at 37°C in hybridization chamber for 40 minutes. After hybridization slides were washed sequentially 3 times each with 50% formamide in 2X SSC

(preheated to 45°C), 0.1X SSC (preheated to 60°C), 4X SSC (0.1% Tween-20), and 2X SSC respectively. Slides were allowed to air dry and mounted using DAPI anti-fade. A minimum 60 metaphase images were captured using Carl Zeiss Axio Imager D2 microscope using 63x Plan Apo 1.4 NA oil immersion objective and analyzed with ImageJ software64 for chromosomal aberrations.

Electron microscopy analysis—EM analysis was performed according to the standard protocol (Zellweger et al., 2015). For DNA extraction, cells were lysed in lysis buffer and digested at 50°C in the presence of Proteinase-K for 2hr. The DNA was purified using chloroform/isoamyl alcohol and precipitated in isopropanol and given 70% ethanol wash and resuspended in elution buffer (TE). Isolated genomic DNA was digested with PvuII HF restriction enzyme for 4 to 5 hr. Replication intermediates were enriched by using QIAGEN G-100 columns (as manufacture's protocol) and concentrated by an Amicon size-exclusion column. The benzyldimethylalkylammonium chloride (BAC) method was used to spread the DNA on the water surface and then loaded on carbon-coated nickel grids and finally DNA was coated with platinum using high-vacuum evaporator MED 010 (Bal Tec). Microscopy was performed with a transmission electron microscope FEI Talos, with 4 K by 4 K cmos camera. For each experimental condition, at least 70 RF intermediates were analyzed per experiment and ImageJ software64 was used to process analyze the images.

DSB detection by PFGE—DSB detection by PFGE was done as reported previously (Cornacchia et al., 2012). Cells were casted into 0.8% agarose plugs (2.5×105 cells/plug), digested in lysis buffer (100 mM EDTA, 1% sodium lauryl sarcosine, 0.2% sodium deoxycholate, 1 mg/ml proteinase-K) at 37°C for 36–40 h, and washed in 10 mM Tris-HCl (pH 8.0)–100 mM EDTA. Electrophoresis was performed at 14°C in 0.9% pulse field-certified agarose (Bio-Rad) using Tris-borate-EDTA buffer in a Bio-Rad Chef DR III apparatus (9 h, 120°, 5.5 V/cm, and 30- to 18 s switch time; 6 h, 117°, 4.5 V/cm, and 18- to 9 s switch time; and 6 h, 112°, 4 V/cm, and 9- to 5 s switch time). The gel was stained with ethidium bromide and imaged on Uvidoc-HD2 Imager. Quantification of DSB was carried out using ImageJ software64. Relative DSB levels were calculated by comparing the results in the treatment conditions to that of the DSB level observed in untreated controls.

***In vivo* studies**—Tumor organoids were collected, incubated with TripLE at 37°C for 10 min, dissociated into single cells, resuspended in tumor organoid medium, filtered with 70μm nilon filters (Corning) and mixed in a in complete mouse media/BME mixture (1:1). KB1P4.N1 and KB1P4.R1 organoid suspensions contained a total of 20.000 and 10.000 cells, respectively, per 40 μl of media/BME mixture, and were injected in the fourth right mammary fat pad of wild-type FVB/N mice. Mammary tumor size was determined by caliper measurements (length and width in millimeters), and tumor volume (in mm^3) was calculated by using the following formula: $0.5 \times$ length $\times$ width^2. Upon tumor outgrowth to approximately 75 mm^3, in mice injected with N1 organoids, and 40 mm^3, in mice injected with R1 organoids, mice were treated with vehicle, or olaparib (50 mg/kg, mice injected with N1 organoids; 100 mg/kg, mice injected with R1 organoids) intraperitoneally for 28 consecutive days. Animals were sacrificed with CO_2 when the tumor volume reached 1,500 mm^3.

Immunohistochemistry analysis—Five-μm tissue sections were cut from formalin-fixed, paraffin-embedded tissue blocks from a cohort of 86 TNBC (Gogola et al., 2018) and 51 human serous ovarian carcinomas (Moudry et al., 2016) and mounted on Super Frost Plus slides (Menzel-Glaser, Braunschweig, Germany), baked at 60°C for 60 min, deparaffinized, and rehydrated through graded alcohol rinses. Heat induced antigen retrieval was performed by immersing the slides in citrate pH 6.0 buffer and heating them in a 750 W microwave oven for 15 min. The sections were then stained with primary antibody anti-LIG3 (1: 250, Sigma-Aldrich, #HPA006723) overnight in a cold-room, followed by subsequent processing by the indirect streptavidin-biotin-peroxidase method using the Vectastain Elite kit (Vector Laboratories, Burlingame, CA, USA) and nickel-sulfate-based chromogen enhancement detection as previously described (Bartkova et al., 2005), without nuclear counterstaining. For negative controls, sections were incubated with non-immune sera. The results were evaluated by two experienced researchers, including a senior oncopathologist, and the data expressed as percentage of positive tumor cells within each lesion, while recording frequencies of cases with LIG3 overabundant (LIG3-high) or lost (LIG3-low) staining in 10%–20% and in excess of 20% of the tumor cells (see Figure 6G for examples of staining patterns). Cases with over 90% of cancer cells showing a staining intensity comparable with surrounding stromal cells on the same section (internal control) were regarded as displaying a normal pattern of LIG 3 expression.

QUANTIFICATION AND STATISTICAL ANALYSIS

Statistical analysis was performed using Prism (GraphPad Software), unless stated in the figure legend. In all cases: ns, non-significant, $* p < 0.05$, $** p < 0.01$, $*** p < 0.001$, $**** p < 0.0001$. For long-term clonogenic and short-term cytotoxicity assays, qRT-PCR and analysis of metaphase spreads, two-tailed unpaired t test was used. For immunofluorescence, unpaired t test was used. For DNA fiber analysis and PLA, group comparisons were performed with Mann–Whitney U test. Analysis of EM was carried out using two-way ANOVA. For survival analysis, data are presented as Kaplan-Meier curves and the p values were computed using Log-Rank (Mantel Cox) statistics.

Supplementary Material

Refer to Web version on PubMed Central for supplementary material.

ACKNOWLEDGMENTS

REFERENCES

Arakawa H, and Iliakis G (2015). Alternative Okazaki fragment ligation pathway by DNA ligase III. Genes (Basel) 6, 385–398. [PubMed: 26110316]

Barazas M, Annunziato S, Pettitt SJ, de Krijger I, Ghezraoui H, Roobol SJ, Lutz C, Frankum J, Song FF, Brough R, et al. (2018). The CST complex mediates end protection at double-strand breaks and promotes PARP inhibitor sensitivity in BRCA1-deficient cells. Cell Rep. 23, 2107–2118. [PubMed: 29768208]

Barazas M, Gasparini A, Huang Y, Küçükosmano lu A, Annunziato S, Bouwman P, Sol W, Kersbergen A, Proost N, de Korte-Grimmerink R, et al. (2019). Radiosensitivity is an acquired vulnerability of PARPi-resistant BRCA1-deficient tumors. Cancer Res. 79, 452–460. [PubMed: 30530501]

Bartkova J, Horejsí Z, Koed K, Krämer A, Tort F, Zieger K, Guldberg P, Sehested M, Nesland JM, Lukas C, et al. (2005). DNA damage response as a candidate anti-cancer barrier in early human tumorigenesis. Nature 434, 864–870. [PubMed: 15829956]

Boersma V, Moatti N, Segura-Bayona S, Peuscher MH, van der Torre J, Wevers BA, Orthwein A, Durocher D, and Jacobs JJL (2015). MAD2L2 controls DNA repair at telomeres and DNA breaks by inhibiting 5′ end resection. Nature 521, 537–540. [PubMed: 25799990]

Bouwman P, Aly A, Escandell JM, Pieterse M, Bartkova J, van der Gulden H, Hiddingh S, Thanasoula M, Kulkarni A, Yang Q, et al. (2010). 53BP1 loss rescues BRCA1 deficiency and is associated with triple-negative and BRCA-mutated breast cancers. Nat. Struct. Mol. Biol. 17, 688–695. [PubMed: 20453858]

Branzei D, and Szakal B (2016). DNA damage tolerance by recombination: Molecular pathways and DNA structures. DNA Repair. (Amst) 44, 68–75. 10.1016/J.DNAREP.2016.05.008. [PubMed: 27236213]

Brinkman EK, Chen T, Amendola M, and van Steensel B (2014). Easy quantitative assessment of genome editing by sequence trace decomposition. Nucleic Acids Res. 42, e168. [PubMed: 25300484]

Brinkman EK, Kousholt AN, Harmsen T, Leemans C, Chen T, Jonkers J, and van Steensel B (2018). Easy quantification of template-directed CRISPR/Cas9 editing. Nucleic Acids Res. 46, e58. [PubMed: 29538768]

Bryant HE, Schultz N, Thomas HD, Parker KM, Flower D, Lopez E, Kyle S, Meuth M, Curtin NJ, and Helleday T (2005). Specific killing of BRCA2-deficient tumours with inhibitors of poly(ADP-ribose) polymerase. Nature 434, 913–917. [PubMed: 15829966]

Bunting SF, Callén E, Wong N, Chen H-T, Polato F, Gunn A, Bothmer A, Feldhahn N, Fernandez-Capetillo O, Cao L, et al. (2010). 53BP1 inhibits homologous recombination in Brca1-deficient cells by blocking resection of DNA breaks. Cell 141, 243–254. [PubMed: 20362325]

Caldecott KW, McKeown CK, Tucker JD, Ljungquist S, and Thompson LH (1994). An interaction between the mammalian DNA repair protein XRCC1 and DNA ligase III. Mol. Cell. Biol. 14, 68–76. [PubMed: 8264637]

Caldecott KW, Aoufouchi S, Johnson P, and Shall S (1996). XRCC1 polypeptide interacts with DNA polymerase β and possibly poly (ADP-ribose) polymerase, and DNA ligase III is a novel molecular 'nick-sensor' in vitro. Nucleic Acids Res. 24, 4387–4394. [PubMed: 8948628]

Cappelli E, Taylor R, Cevasco M, Abbondandolo A, Caldecott K, and Frosina G (1997). Involvement of XRCC1 and DNA ligase III gene products in DNA base excision repair. J. Biol. Chem. 272, 23970–23975. [PubMed: 9295348]

Ceccaldi R, Liu JC, Amunugama R, Hajdu I, Primack B, Petalcorin MI, O'Connor KW, Konstantinopoulos PA, Elledge SJ, Boulton SJ, et al. (2015). Homologous-recombination-deficient tumours are dependent on Polθ-mediated repair. Nature 518, 258–262. [PubMed: 25642963]

Chapman JR, Barral P, Vannier JB, Borel V, Steger M, Tomas-Loba A, Sartori AA, Adams IR, Batista FD, and Boulton SJ (2013). RIF1 is essential for 53BP1-dependent nonhomologous end joining and suppression of DNA double-strand break resection. Mol. Cell 49, 858–871. [PubMed: 23333305]

Cong L, Ran FA, Cox D, Lin S, Barretto R, Habib N, Hsu PD, Wu X, Jiang W, Marraffini LA, and Zhang F (2013). Multiplex genome engineering using CRISPR/Cas systems. Science 339, 819–823. [PubMed: 23287718]

Cong K, Peng M, Kousholt AN, Lee WTC, Lee S, Nayak S, Krais J, VanderVere-Carozza PS, Pawelczak KS, Calvo J, et al. (2021). Replication gaps are a key determinant of PARP inhibitor synthetic lethality with BRCA deficiency. Mol. Cell 81, 3128–3144.e7. [PubMed: 34216544]

Cornacchia D, Dileep V, Quivy JP, Foti R, Tili F, Santarella-Mellwig R, Antony C, Almouzni G, Gilbert DM, and Buonomo SBC (2012). Mouse Rif1 is a key regulator of the replication-timing programme in mammalian cells. EMBO J. 31, 3678–3690. [PubMed: 22850673]

Dev H, Chiang T-WW, Lescale C, de Krijger I, Martin AG, Pilger D, Coates J, Sczaniecka-Clift M, Wei W, Ostermaier M, et al. (2018). Shieldin complex promotes DNA end-joining and counters homologous recombination in BRCA1-null cells. Nat. Cell Biol. 20, 954–965. [PubMed: 30022119]

Drost R, Dhillon KK, van der Gulden H, van der Heijden I, Brandsma I, Cruz C, Chondronasiou D, Castroviejo-Bermejo M, Boon U, Schut E, et al. (2016). BRCA1185delAG tumors may acquire therapy resistance through expression of RING-less BRCA1. J. Clin. Invest. 126, 2903–2918. [PubMed: 27454287]

Duarte AA, Gogola E, Sachs N, Barazas M, Annunziato S, R de Ruiter J, Velds A, Blatter S, Houthuijzen JM, van de Ven M, et al. (2018). BRCA-deficient mouse mammary tumor organoids to study cancer-drug resistance. Nat. Methods 15, 134–140. [PubMed: 29256493]

Escribano-Díaz C, Orthwein A, Fradet-Turcotte A, Xing M, Young JTF, Tká J, Cook MA, Rosebrock AP, Munro M, Canny MD, et al. (2013). A cell cycle-dependent regulatory circuit composed of 53BP1-RIF1 and BRCA1-CtIP controls DNA repair pathway choice. Mol. Cell 49, 872–883. [PubMed: 23333306]

Evers B, Drost R, Schut E, de Bruin M, van der Burg E, Derksen PWB, Holstege H, Liu X, van Drunen E, Beverloo HB, et al. (2008). Selective inhibition of BRCA2-deficient mammary tumor cell growth by AZD2281 and cisplatin. Clin. Cancer Res. 14, 3916–3925. [PubMed: 18559613]

Farmer H, McCabe N, Lord CJ, Tutt AN, Johnson DA, Richardson TB, Santarosa M, Dillon KJ, Hickson I, Knights C, et al. (2005). Targeting the DNA repair defect in BRCA mutant cells as a therapeutic strategy. Nature 434, 917–921. [PubMed: 15829967]

Follenzi A, Ailles LE, Bakovic S, Geuna M, and Naldini L (2000). Gene transfer by lentiviral vectors is limited by nuclear translocation and rescued by HIV-1 pol sequences. Nat. Genet. 25, 217–222. [PubMed: 10835641]

Fumasoni M, Zwicky K, Vanoli F, Lopes M, and Branzei D (2015). Error-free DNA damage tolerance and sister chromatid proximity during DNA replication rely on the Polα/primase/Ctf4 complex. Mol. Cell 57, 812–823. [PubMed: 25661486]

García-Gómez S, Reyes A, Martínez-Jiménez MI, Chocrón ES, Mourón S, Terrados G, Powell C, Salido E, Méndez J, Holt IJ, and Blanco L (2013). PrimPol, an archaic primase/polymerase operating in human cells. Mol. Cell 52, 541–553. [PubMed: 24207056]

Ghezraoui H, Oliveira C, Becker JR, Bilham K, Moralli D, Anzilotti C, Fischer R, Deobagkar-Lele M, Sanchiz-Calvo M, Fueyo-Marcos E, et al. (2018). 53BP1 cooperation with the REV7-shieldin complex underpins DNA structure-specific NHEJ. Nature 560, 122–127. [PubMed: 30046110]

Gogola E, Duarte AA, de Ruiter JR, Wiegant WW, Schmid JA, de Bruijn R, James DI, Guerrero Llobet S, Vis DJ, Annunziato S, et al. (2018). Selective loss of PARG restores PARylation and counteracts PARP inhibitor-mediated synthetic lethality. Cancer Cell 33, 1078–1093.e12. [PubMed: 29894693]

Hanzlikova H, Kalasova I, Demin AA, Pennicott LE, Cihlarova Z, and Caldecott KW (2018). The importance of poly(ADP-ribose) polymerase as a sensor of unligated Okazaki fragments during DNA replication. Mol. Cell 71, 319–331.e3. [PubMed: 29983321]

Hashimoto Y, Ray Chaudhuri A, Lopes M, and Costanzo V (2010). Rad51 protects nascent DNA from Mre11-dependent degradation and promotes continuous DNA synthesis. Nat. Struct. Mol. Biol. 17, 1305–1311. [PubMed: 20935632]

Helleday T (2011). The underlying mechanism for the PARP and BRCA synthetic lethality: clearing up the misunderstandings. Mol. Oncol. 5, 387–393. [PubMed: 21821475]

Ianevski A, Giri AK, and Aittokallio T (2020). SynergyFinder 2.0: visual analytics of multi-drug combination synergies. Nucleic Acids Res. 48 (W1), W488–W493. [PubMed: 32246720]

James DI, Smith KM, Jordan AM, Fairweather EE, Griffiths LA, Hamilton NS, Hitchin JR, Hutton CP, Jones S, Kelly P, et al. (2016). First-in-class chemical probes against poly(ADP-ribose) glycohydrolase (PARG) inhibit DNA repair with differential pharmacology to olaparib. ACS Chem. Biol. 11, 3179–3190. [PubMed: 27689388]

Jaspers JE, Kersbergen A, Boon U, Sol W, van Deemter L, Zander SA, Drost R, Wientjens E, Ji J, Aly A, et al. (2013). Loss of 53BP1 causes PARP inhibitor resistance in Brca1-mutated mouse mammary tumors. Cancer Discov. 3, 68–81. [PubMed: 23103855]

Lakshmipathy U, and Campbell C (1999). The human DNA ligase III gene encodes nuclear and mitochondrial proteins. Mol. Cell. Biol. 19, 3869–3876. [PubMed: 10207110]

Li W, Xu H, Xiao T, Cong L, Love MI, Zhang F, Irizarry RA, Liu JS, Brown M, and Liu XS (2014). MAGeCK enables robust identification of essential genes from genome-scale CRISPR/Cas9 knockout screens. Genome Biol. 15, 554. [PubMed: 25476604]

Love MI, Huber W, and Anders S (2014). Moderated estimation of fold change and dispersion for RNA-seq data with DESeq2. Genome Biol. 15, 550. [PubMed: 25516281]

Lupo B, and Trusolino L (2014). Inhibition of poly(ADP-ribosyl)ation in cancer: old and new paradigms revisited. Biochim. Biophys. Acta 1846, 201–215. [PubMed: 25026313]

Mateos-Gomez PA, Gong F, Nair N, Miller KM, Lazzerini-Denchi E, and Sfeir A (2015). Mammalian polymerase θ promotes alternative NHEJ and suppresses recombination. Nature 518, 254–257. [PubMed: 25642960]

Maya-Mendoza A, Moudry P, Merchut-Maya JM, Lee M, Strauss R, and Bartek J (2018). High speed of fork progression induces DNA replication stress and genomic instability. Nature 559, 279–284. [PubMed: 29950726]

McQuin C, Goodman A, Chernyshev V, Kamentsky L, Cimini BA, Karhohs KW, Doan M, Ding L, Rafelski SM, Thirstrup D, et al. (2018). CellProfiler 3.0: next-generation image processing for biology. PLoS Biol. 16, e2005970. [PubMed: 29969450]

Moudry P, Watanabe K, Wolanin KM, Bartkova J, Wassing IE, Watanabe S, Strauss R, Troelsgaard Pedersen R, Oestergaard VH, Lisby M, et al. (2016). TOPBP1 regulates RAD51 phosphorylation and chromatin loading and determines PARP inhibitor sensitivity. J. Cell Biol. 212, 281–288. [PubMed: 26811421]

Mukherjee C, Tripathi V, Manolika EM, Heijink AM, Ricci G, Merzouk S, de Boer HR, Demmers J, van Vugt MATM, and Ray Chaudhuri A (2019). RIF1 promotes replication fork protection and efficient restart to maintain genome stability. Nat. Commun. 10, 3287. [PubMed: 31337767]

Murai J, Huang SYN, Das BB, Renaud A, Zhang Y, Doroshow JH, Ji J, Takeda S, and Pommier Y (2012). Trapping of PARP1 and PARP2 by clinical PARP inhibitors. Cancer Res. 72, 5588–5599. [PubMed: 23118055]

Murai J, Huang SYN, Renaud A, Zhang Y, Ji J, Takeda S, Morris J, Teicher B, Doroshow JH, and Pommier Y (2014). Stereospecific PARP trapping by BMN 673 and comparison with olaparib and rucaparib. Mol. Cancer Ther. 13, 433–443. [PubMed: 24356813]

Noordermeer SM, Adam S, Setiaputra D, Barazas M, Pettitt SJ, Ling AK, Olivieri M, Álvarez-Quilón A, Moatti N, Zimmermann M, et al. (2018). The shieldin complex mediates 53BP1-dependent DNA repair. Nature 560, 117–121. [PubMed: 30022168]

Paes Dias M, Moser SC, Ganesan S, and Jonkers J (2021). Understanding and overcoming resistance to PARP inhibitors in cancer therapy. Nat. Rev. Clin. Oncol. Published online July 20, 2021. 10.1038/s41571-021-00532-x.

Panzarino NJ, Krais JJ, Cong K, Peng M, Mosqueda M, Nayak SU, Bond SM, Calvo JA, Doshi MB, Bere M, et al. (2021). Replication gaps underlie BRCA deficiency and therapy response. Cancer Res. 81, 1388–1397. [PubMed: 33184108]

Pascal JM, and Ellenberger T (2015). The rise and fall of poly(ADP-ribose): an enzymatic perspective. DNA Repair (Amst.) 32, 10–16. [PubMed: 25963443]

Peng M, Cong K, Panzarino NJ, Nayak S, Calvo J, Deng B, Zhu LJ, Morocz M, Hegedus L, Haracska L, and Cantor SB (2018). Opposing roles of FANCJ and HLTF protect forks and restrain replication during stress. Cell Rep. 24, 3251–3261. [PubMed: 30232006]

Pettitt SJ, Rehman FL, Bajrami I, Brough R, Wallberg F, Kozarewa I, Fenwick K, Assiotis I, Chen L, Campbell J, et al. (2013). A genetic screen using the PiggyBac transposon in haploid cells identifies Parp1 as a mediator of olaparib toxicity. PLoS ONE 8, e61520. [PubMed: 23634208]

Pettitt SJ, Krastev DB, Brandsma I, Dréan A, Song F, Aleksandrov R, Harrell MI, Menon M, Brough R, Campbell J, et al. (2018). Genome-wide and high-density CRISPR-Cas9 screens identify point mutations in PARP1 causing PARP inhibitor resistance. Nat. Commun. 9, 1849. [PubMed: 29748565]

Piberger AL, Bowry A, Kelly RDW, Walker AK, González-Acosta D, Bailey LJ, Doherty AJ, Méndez J, Morris JR, Bryant HE, and Petermann E (2020). PrimPol-dependent single-stranded gap formation mediates homologous recombination at bulky DNA adducts. Nat. Commun. 11, 5863. [PubMed: 33203852]

Puebla-Osorio N, Lacey DB, Alt FW, and Zhu C (2006). Early embryonic lethality due to targeted inactivation of DNA ligase III. Mol. Cell. Biol. 26, 3935–3941. [PubMed: 16648486]

Quinet A, Tirman S, Jackson J, Švikovi S, Lemaçon D, Carvajal-Maldonado D, González-Acosta D, Vessoni AT, Cybulla E, Wood M, et al. (2020). PRIMPOL-mediated adaptive response suppresses replication fork reversal in BRCA-deficient cells. Mol. Cell 77, 461–474.e9. [PubMed: 31676232]

Ray Chaudhuri A, and Nussenzweig A (2017). The multifaceted roles of PARP1 in DNA repair and chromatin remodelling. Nat. Rev. Mol. Cell Biol. 18, 610–621. [PubMed: 28676700]

Ray Chaudhuri A, Hashimoto Y, Herrador R, Neelsen KJ, Fachinetti D, Bermejo R, Cocito A, Costanzo V, and Lopes M (2012). Topoisomerase I poisoning results in PARP-mediated replication fork reversal. Nat. Struct. Mol. Biol. 19, 417–423. [PubMed: 22388737]

Ray Chaudhuri A, Callen E, Ding X, Gogola E, Duarte AA, Lee J-E, Wong N, Lafarga V, Calvo JA, Panzarino NJ, et al. (2016). Replication fork stability confers chemoresistance in BRCA-deficient cells. Nature 535, 382–387. [PubMed: 27443740]

Rottenberg S, Jaspers JE, Kersbergen A, van der Burg E, Nygren AOH, Zander SAL, Derksen PWB, de Bruin M, Zevenhoven J, Lau A, et al. (2008). High sensitivity of BRCA1-deficient mammary tumors to the PARP inhibitor AZD2281 alone and in combination with platinum drugs. Proc. Natl. Acad. Sci. USA 105, 17079–17084. [PubMed: 18971340]

Rueden CT, Schindelin J, Hiner MC, DeZonia BE, Walter AE, Arena ET, and Eliceiri KW (2017). ImageJ2: ImageJ for the next generation of scientific image data. BMC Bioinformatics 18, 529. [PubMed: 29187165]

Sanjana NE, Shalem O, and Zhang F (2014). Improved vectors and genome-wide libraries for CRISPR screening. Nat. Methods 11, 783–784. [PubMed: 25075903]

Schlacher K, Christ N, Siaud N, Egashira A, Wu H, and Jasin M (2011). Double-strand break repair-independent role for BRCA2 in blocking stalled replication fork degradation by MRE11. Cell 145, 529–542. [PubMed: 21565612]

Simsek D, Furda A, Gao Y, Artus J, Brunet E, Hadjantonakis A-K, Van Houten B, Shuman S, McKinnon PJ, and Jasin M (2011). Crucial role for DNA ligase III in mitochondria but not in Xrcc1-dependent repair. Nature 471, 245–248. [PubMed: 21390132]

Sriramachandran AM, Petrosino G, Méndez-Lago M, Schäfer AJ, Batista-Nascimento LS, Zilio N, and Ulrich HD (2020). Genome-wide nucleotide-resolution mapping of DNA replication patterns, single-strand breaks, and lesions by GLOE-Seq. Mol. Cell 78, 975–985.e7. [PubMed: 32320643]

Taglialatela A, Alvarez S, Leuzzi G, Sannino V, Ranjha L, Huang J-W, Madubata C, Anand R, Levy B, Rabadan R, et al. (2017). Restoration of replication fork stability in BRCA1- and BRCA2-deficient cells by inactivation of SNF2-family fork remodelers. Mol. Cell 68, 414–430.e8. [PubMed: 29053959]

Taylor RM, Whitehouse CJ, and Caldecott KW (2000). The DNA ligase III zinc finger stimulates binding to DNA secondary structure and promotes end joining. Nucleic Acids Res. 28, 3558–3563. [PubMed: 10982876]

Toledo LI, Altmeyer M, Rask M-B, Lukas C, Larsen DH, Povlsen LK, Bekker-Jensen S, Mailand N, Bartek J, and Lukas J (2013). ATR prohibits replication catastrophe by preventing global exhaustion of RPA. Cell 155, 1088–1103. [PubMed: 24267891]

Wang H, Rosidi B, Perrault R, Wang M, Zhang L, Windhofer F, and Iliakis G (2005). DNA ligase III as a candidate component of backup pathways of nonhomologous end joining. Cancer Res. 65, 4020–4030. [PubMed: 15899791]

Xu G, Chapman JR, Brandsma I, Yuan J, Mistrik M, Bouwman P, Bartkova J, Gogola E, Warmerdam D, Barazas M, et al. (2015). REV7 counteracts DNA double-strand break resection and affects PARP inhibition. Nature 521, 541–544. [PubMed: 25799992]

Yoshimi K, Kunihiro Y, Kaneko T, Nagahora H, Voigt B, and Mashimo T (2016). ssODN-mediated knock-in with CRISPR-Cas for large genomic regions in zygotes. Nat. Commun. 7, 10431. [PubMed: 26786405]

Zatreanu D, Robinson HMR, Alkhatib O, Boursier M, Finch H, Geo L, Grande D, Grinkevich V, Heald RA, Langdon S, et al. (2021). Polθ inhibitors elicit BRCA-gene synthetic lethality and target PARP inhibitor resistance. Nat. Commun. 12, 3636. [PubMed: 34140467]

Zellweger R, Dalcher D, Mutreja K, Berti M, Schmid JA, Herrador R, Vindigni A, and Lopes M (2015). Rad51-mediated replication fork reversal is a global response to genotoxic treatments in human cells. J. Cell Biol. 208, 563–579. [PubMed: 25733714]

Zhou J, Gelot C, Pantelidou C, Li A, Yucel H, Davis RE, Farkkila A, Kochupurakkal B, Syed A, Shapiro GI, et al. (2020). Polymerase theta inhibition kills homologous recombination deficient tumors. bioRxiv. 10.1101/2020.05.23.111658.

Highlights

- LIG3 is a critical suppressor of PARPi toxicity in BRCA1$^{-/-}$53BP1$^{-/-}$ cells

- Enhanced PARPi toxicity by LIG3 depletion requires BRCA1 loss but not HR deficiency

- LIG3 loss induces MRE11-mediated ssDNA gaps in BRCA1$^{-/-}$53BP1$^{-/-}$ cells exposed to PARPi

- LIG3 depletion enhances efficacy of PARPi against BRCA1-deficient mouse mammary tumors
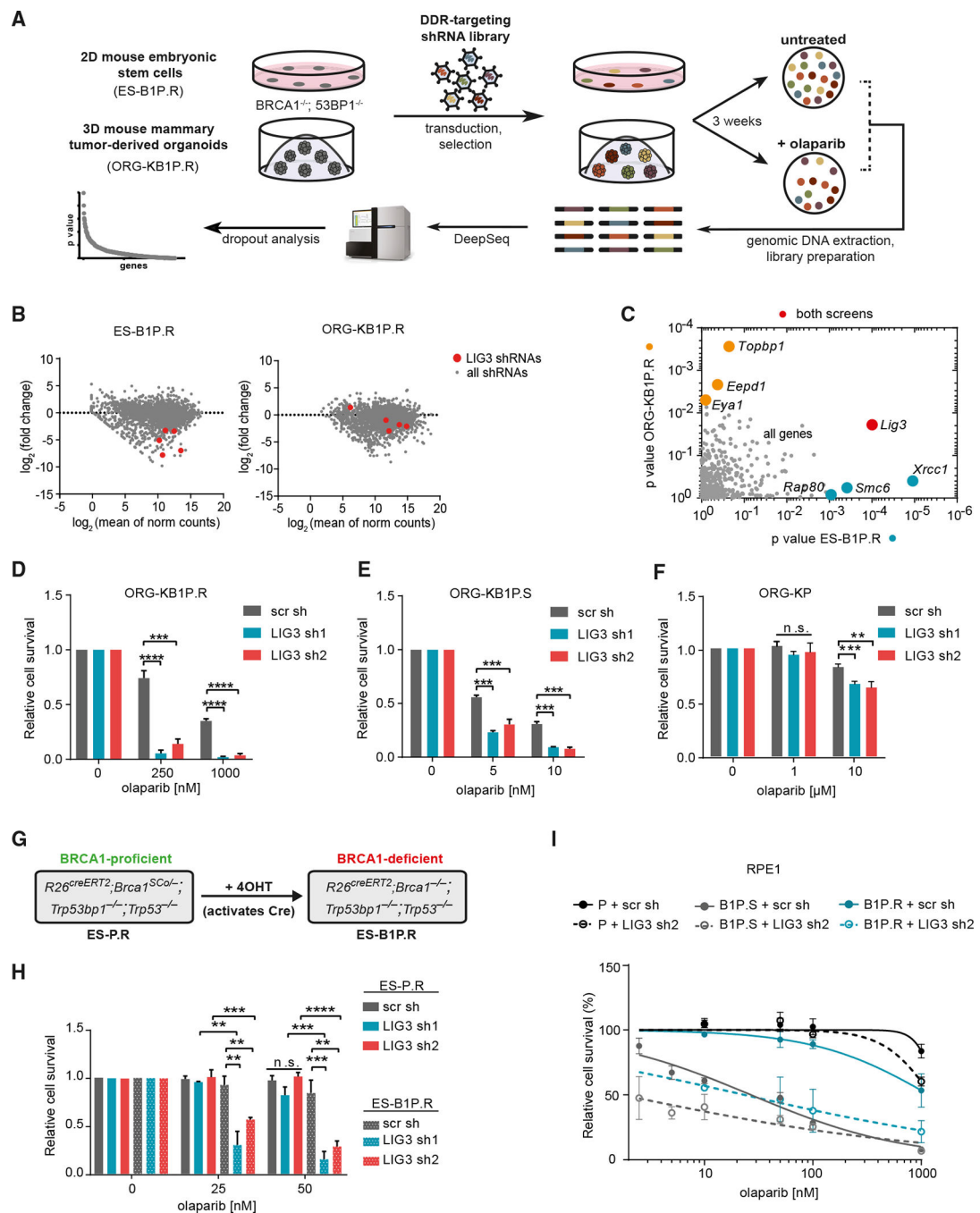
Figure 1. Depletion of LIG3 increases sensitivity to PARPi in BRCA1-deficient cells, independent of 53BP1 loss

(A) Outline of shRNA dropout screens. Screens were done at olaparib concentrations of 25 and 50 nM for ES-B1P.R and ORG-KB1P.R, respectively.

(B) Plot of $\log_2$ ratio (fold change [treated versus untreated]) versus abundance (mean of normalized [norm] counts) of shRNAs extracted from ES-B1P.R mESCs and ORG-KB1P.R organoids treated with olaparib or left untreated for 3 weeks. To eliminate artifacts of significant cell death without PARPi, the analysis considered fold change between untreated

and treated conditions and removed genes that were already depleted at T0 (day of seeding). Analyzed using MAGeCK.

(C) Comparison of the screening outcome between indicated cell lines. p value by MAGeCK.

(D–F) Quantification of long-term clonogenic assays with ORG-KB1P.R (D), ORG-KB1P.S (E), and ORG-KP organoids (F) treated with olaparib or left untreated.

(G) Schematic representation of the *Brca1* selectable conditional allele in $R26^{creERT2};Brca1^{SCo/-};Trp53bp1^{-/-};Trp53^{-/-}$ (ES-P.R) mESCs. Incubation of these cells with 4-hydroxytamoxifen (4OHT) induces CreERT2 recombinase, resulting in $R26^{creERT2};Brca1^{-/-};Trp53bp1^{-/-};Trp53^{-/-}$ (ES-B1P.R) cells lacking BRCA1.

(H) Quantification of long-term clonogenic assay in ES-P.R and ES-B1P.R cells treated with olaparib. See also Figure S2.

(I) Quantification of long-term clonogenic assays in RPE1-P, RPE1-B1P.S and RPE1-B1P.R cells treated with olaparib. See also Figure S2.

Data are represented as mean ± SD. **p < 0.01, ***p < 0.001, and ****p < 0.0001; n.s., not significant (two-tailed t test).
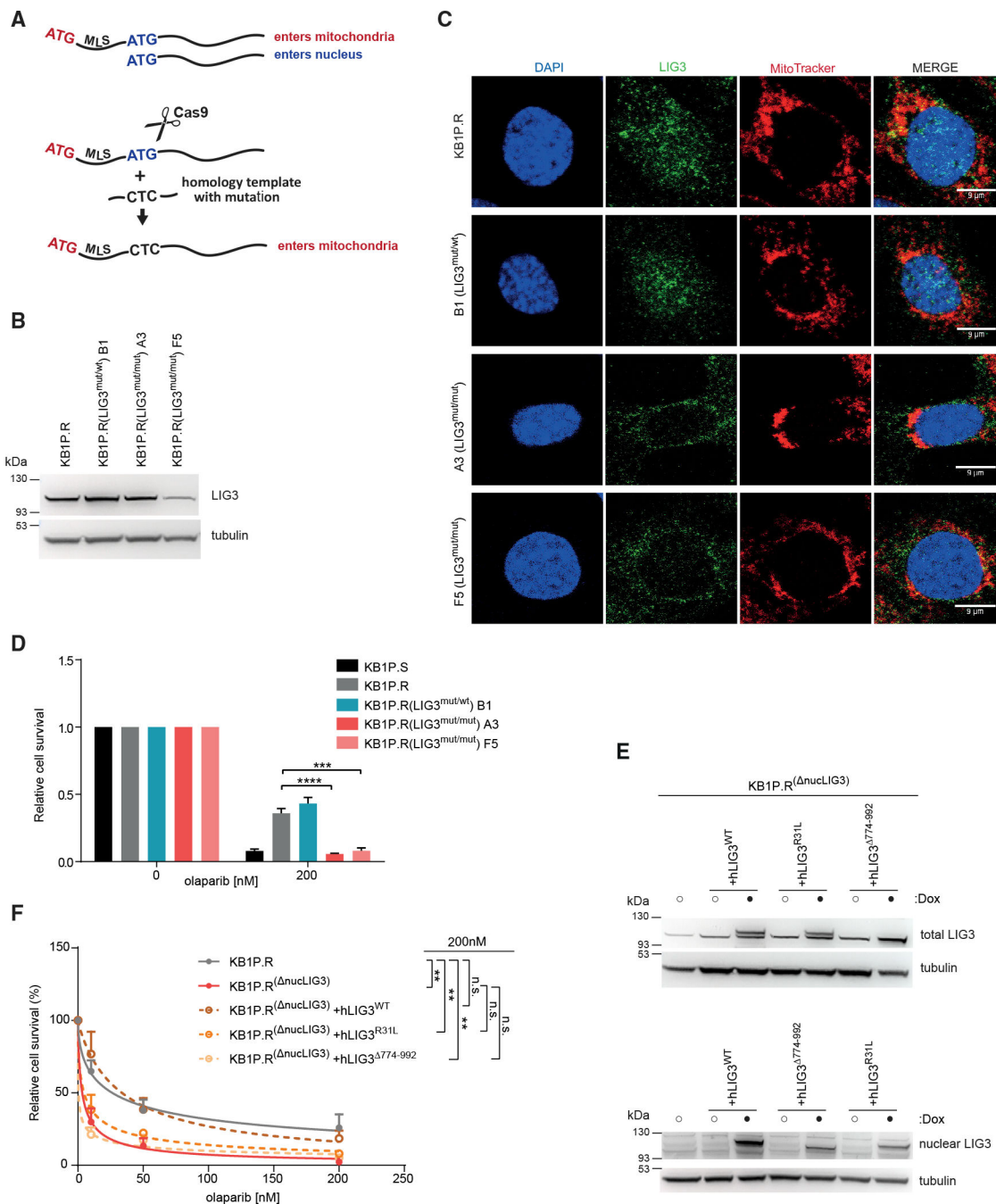
Figure 2. Resistance to PARPi in 53BP1-deficient KB1P cells is mediated by nuclear LIG3

(A) Generation of nuclear LIG3 mutants in KB1P.R cells. *Lig3* contains two ATG translation initiation sites flanking a mitochondrial targeting sequence (MLS). Translation initiated at the upstream ATG site produces a mitochondrial protein, whereas translation from the downstream ATG site produces the nuclear form. Ablation of the downstream ATG allows cells to retain mitochondrial, but not nuclear LIG3 function. CRISPR-Cas9 was used to introduce in-frame ATG > CTC mutation in the nuclear ATG through delivery of a homology repair template.

(B) Western blot analysis of LIG3 in whole-cell lysates of KB1P.R, KB1P.R(LIG3$^{mut/wt}$) B1, KB1P.R(LIG3$^{mut/mut}$) A3, and KB1P.R(LIG3$^{mut/mut}$) F5 cells.

(C) LG3 immunofluorescence and MitoTracker staining in nuclear LIG3 mutant cells. Scale bar, 9 μm.

(D) Quantification of long-term clonogenic assays with KB1P.S, KB1P.R cells, and nuclear LIG3 mutant clones B1, A3, and F5, treated with olaparib or untreated.

(E) Western blot analysis of total and nuclear LIG3 in KB1P.R and nuclear LIG3 mutant KB1P.R$^{(\;nucLIG3)}$ cells. Expression of LIG3 constructs was induced with doxycycline (Dox) for 2 days prior to analysis.

(F) Quantification of long-term clonogenic assay with KB1P.R and nuclear LIG3 mutant KB1P.R$^{(\;nucLIG3)}$ cells, treated with olaparib or untreated. Expression of LIG3 constructs was induced with doxycycline (Dox) starting 2 days before the assay and maintained for the duration of the assay.

Data are represented as mean ± SD. **p < 0.01, ***p < 0.001, and ****p < 0.0001; n.s., not significant (two-tailed t test).
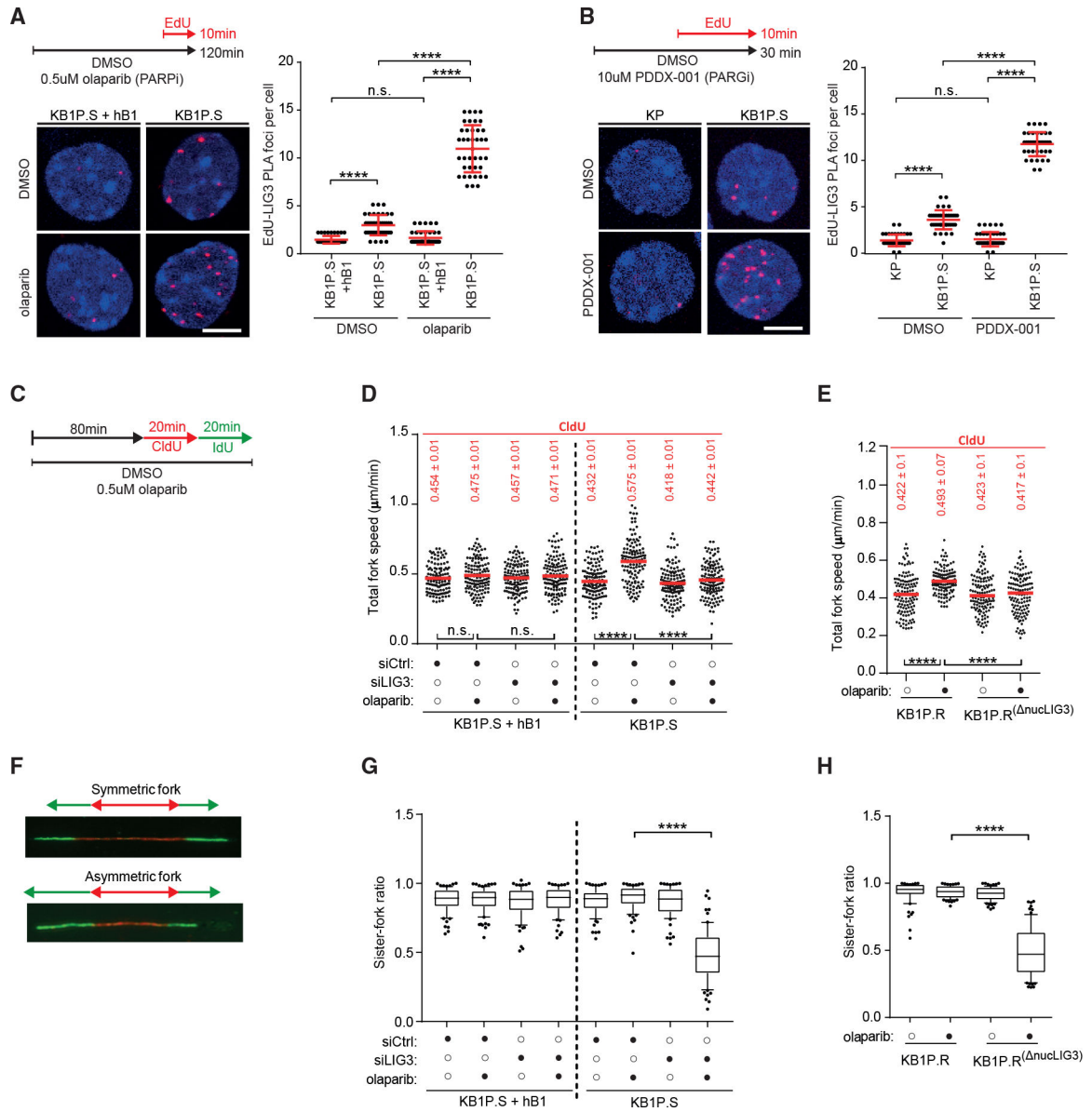
Figure 3. LIG3 is required at replication forks in BRCA1-deficient cells treated with PARPi
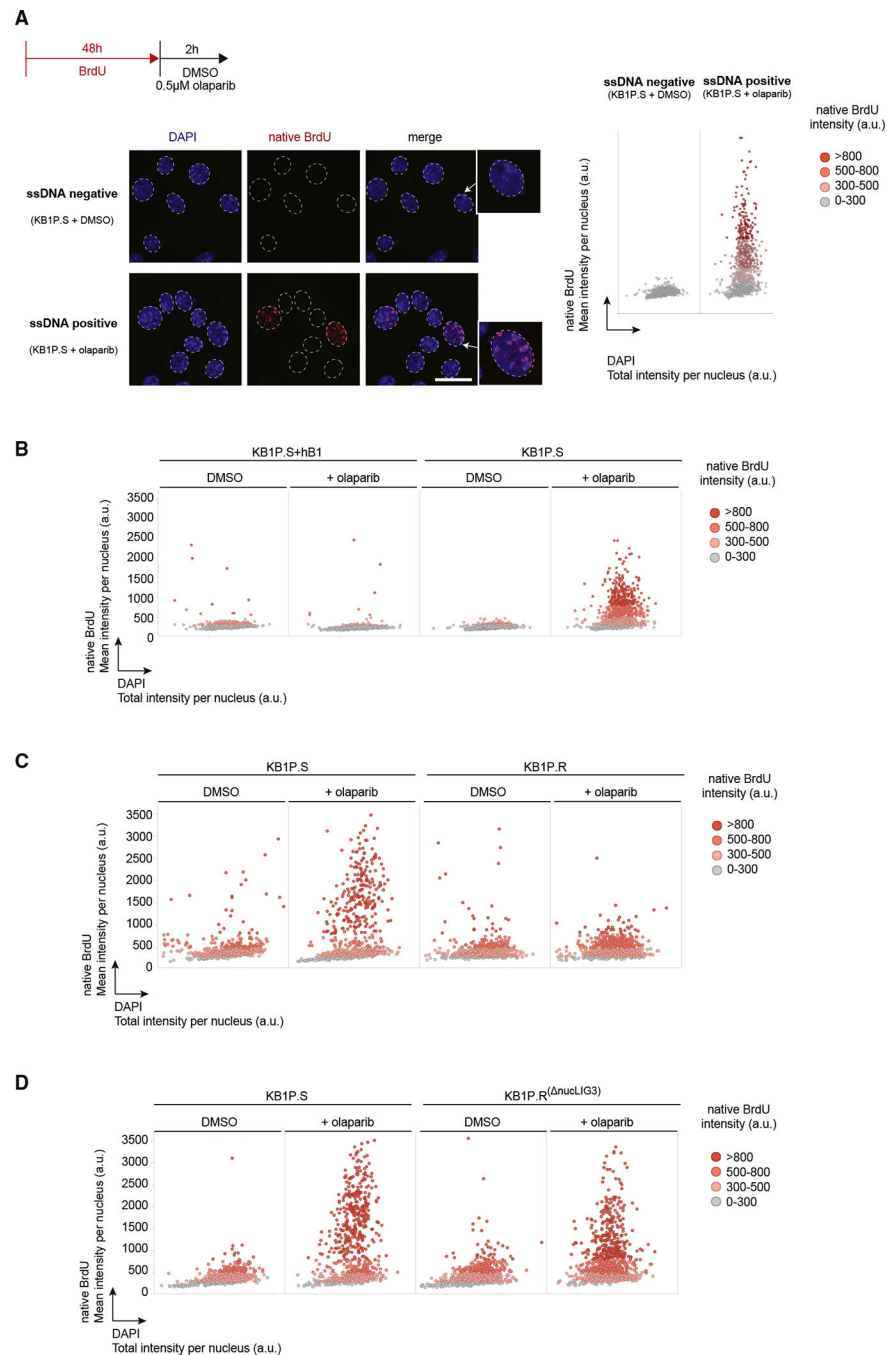
(A) Experimental setup, representative images, and quantification of LIG3-EdU proximity ligation assay (PLA) foci in KB1P.S+hB1 and KB1P.S cells incubated for 10 min with 20 μM EdU, in the absence or presence of olaparib. Scale bar, 5 μm.

(B) Experimental setup, representative images, and quantification of LIG3-EdU PLA foci in KP and KB1P.S cells incubated for 10 min with 20 μM EdU, in the absence or presence of PDDX-001. Scale bar, 5 μm.

(C) Experimental setup of DNA fiber assay. Cells were pre-incubated with 0.5 μM olaparib for 80 min, followed by sequential labeling with CldU (red) and IdU (green) in the presence of olaparib for 20 min each. RF progression was quantified by measuring tract lengths of CldU and IdU in micrometers.

(D) Quantification of RF speed in CldU tracks, following the indicated treatments, in KB1P.S+hB1 and KB1P.S cells after siRNA-mediated depletion of LIG3. See also Figure S6.

(E) Quantification of RF speed in CldU tracks, following the indicated treatments, in nuclear LIG3 mutant KB1P.R$^{(\ nucLIG3)}$ cells. See also Figure S6.

(F) Representative images of symmetric and asymmetric RFs.

(G) Quantification of RF symmetry following the indicated treatments in KB1P.R cells. The box represents the 10th to 90th percentile range.

(H) Quantification of RF symmetry following the indicated treatments in KB1P.R and KB1P.R$^{(\ nucLIG3)}$ cells. The box represents the 10th to 90th percentile range.

Data are represented as mean. ****p < 0.0001; n.s., not significant (Mann-Whitney U test).

Figure 4. Loss of LIG3 in BRCA1-deficient cells results in an increase in PARPi-mediated ssDNA regions

(A) Experimental setup to quantify amount of ssDNA gaps per nucleus by quantitative image-based cytometry (QIBC) analysis of mean intensity of native BrdU per nucleus. Cells were incubated with BrdU for 48 h followed by 2 h treatment with 0.5 μM olaparib or left untreated. Scale bar, 50 μm.

(B–D) QIBC analysis of ssDNA in KB1P.S+hB1 and KB1P.S cells (B), KB1P.S and KB1P.R cells (C), and KB1P.S and KB1P.R$^{(\Delta nucLIG3)}$ cells (D).

See also Figure S7.
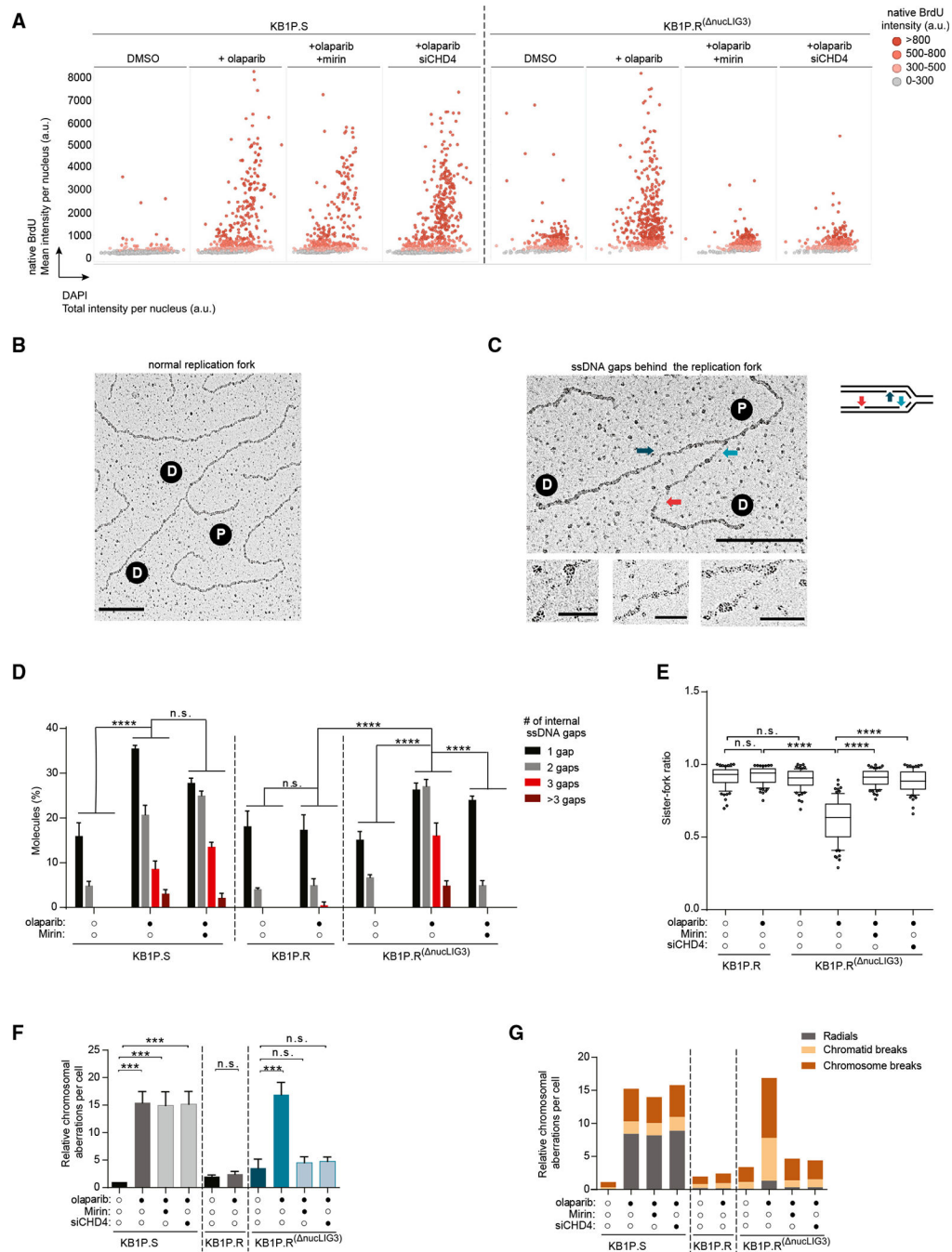
Figure 5. Increase in ssDNA gaps results in increased genomic instability in LIG3-deficient cells

(A) QIBC analysis of ssDNA gaps in KB1P.S and nuclear LIG3 mutant KB1P.R$^{(\Delta nucLIG3)}$ cells. Cells were treated with 25 μM mirin for 48 h prior to treatment with olaparib or transfected with siRNA targeting CHD4. See also Figure S7.

(B and C) Representative electron micrographs of normal RF (B) and RF with internal ssDNA gaps behind the fork (C). Scale bar for large panels: 250 nm = 1,214 bp; scale bar for small panels: 50 nm = 242 bp. P, parental strand; D, daughter strand.

(D) Quantification of internal ssDNA gaps behind RFs observed in KB1P.S, KB1P.R, and KB1P.R$^{(nucLIG3)}$ cells upon treatment with 0.5 μM olaparib for 2 h. KB1P.S and KB1P.R$^{(nucLIG3)}$ cells were additionally treated with 25 μM mirin for 48 h prior to treatment with olaparib or transfected with siRNA targeting CHD4. Data were acquired using electron microscopy. Data are represented as mean ± SD. ****p < 0.0001; n.s., not significant (two-way ANOVA).

(E) Quantification of RF symmetry in KB1P.R and KB1P.R$^{(nucLIG3)}$ cells following indicated treatments. KB1P.R$^{(nucLIG3)}$ cells were additionally treated with 25 μM mirin for 48 h prior to treatment with olaparib, or transfected with siRNA targeting CHD4. Data are represented as mean, and the box represents the 10th to 90th percentile range. ****p < 0.0001; n.s., not significant (Mann-Whitney U test).

(F) Quantification of chromosomal aberrations in KB1P.S, KB1P.R, and KB1P.R$^{(nucLIG3)}$ cells following 2 h treatment with 0.5 μM olaparib and recovery for 6 h. KB1P.S and KB1P.R$^{(nucLIG3)}$ cells were additionally treated with 25 μM mirin for 48 h prior to treatment with olaparib or transfected with siRNA targeting CHD4. Data are represented as mean ± SD. ***p < 0.001; n.s., not significant (two-tailed t test).

(G) Quantification of the different types of chromosomal aberrations identified in (F).
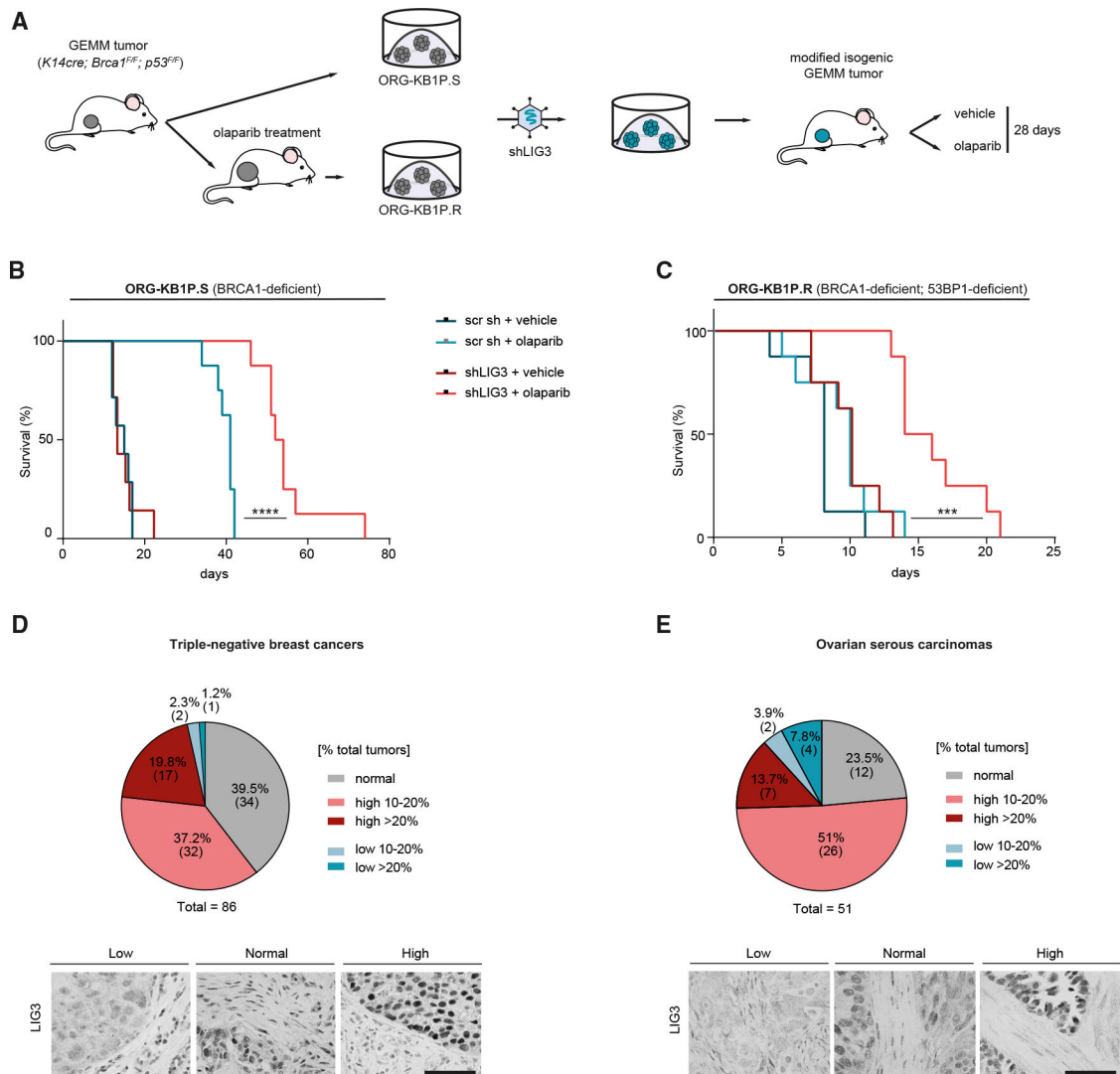
Figure 6. LIG3 depletion increases *in vivo* efficacy of PARPi and is overexpressed in a fraction of human tumors

(A) Outline of *in vivo* experimental set up. Organoids were modified *in vitro* and transplanted into the mammary fat pad of syngeneic, wild-type FVB/NRj mice. Upon tumor outgrowth, mice were treated with olaparib or vehicle for 28 consecutive days.

(B and C) Kaplan-Meier survival curves of mice transplanted with KB1P.S (B) or KB1P.R organoid lines (C), after *in vitro* shRNA-mediated depletion of LIG3. ***p < 0.001 and ****p < 0.0001 (log rank [Mantel-Cox]).

(D and E) Summary and representative images of immunohistochemistry (IHC) analysis of LIG3 expression in triple-negative breast cancers (D) and ovarian serous carcinomas (E). Scale bar, 100 μM.
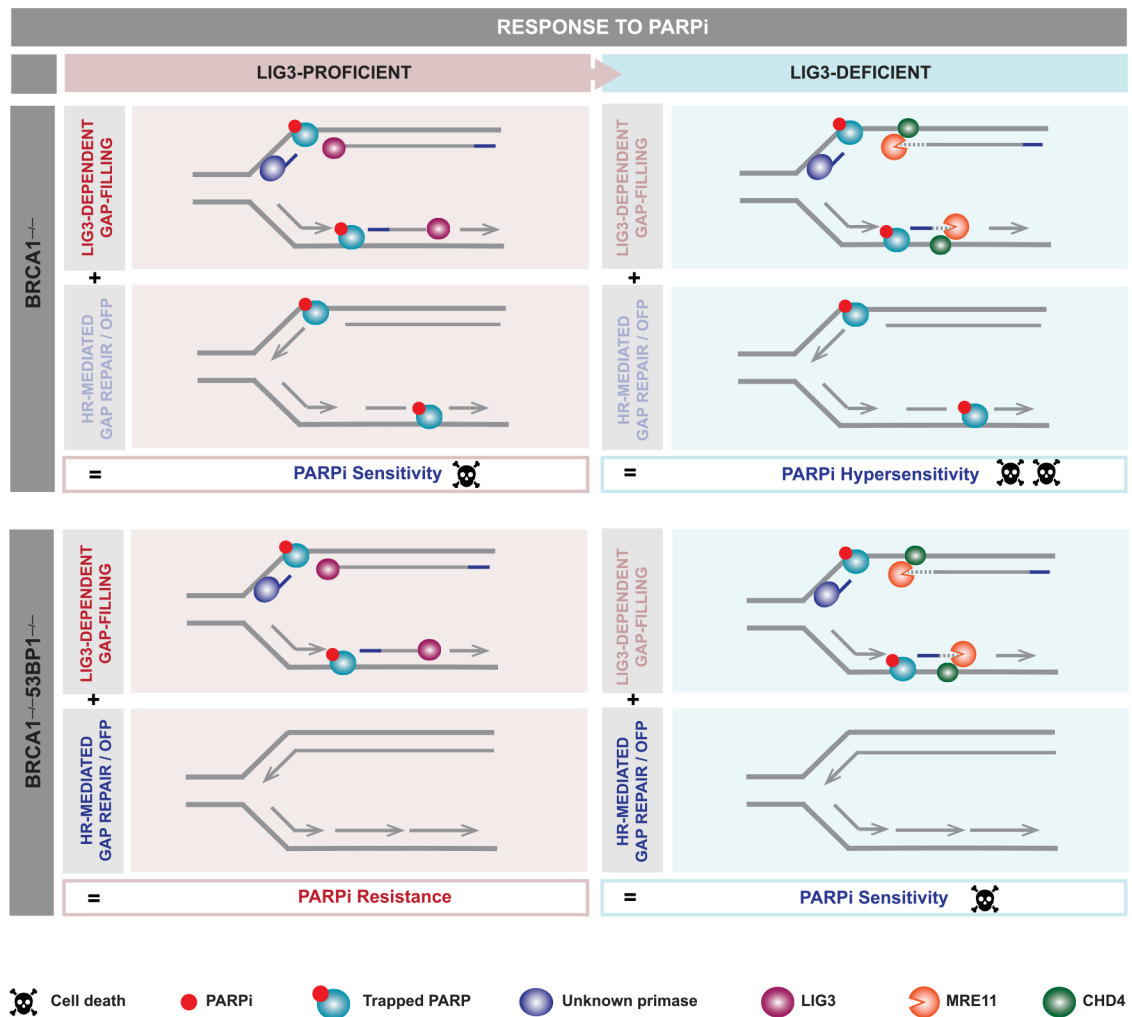
Figure 7. Proposed model

BRCA1-deficient cells can bypass chromatin-trapped PARP1 lesions via two different mechanisms of gap suppression: one dependent on loss of 53BP1 and another that is LIG3 dependent. 53BP1-mediated ssDNA gap induction may result from loss of HR-mediated gap repair and/or defective Okazaki fragment processing. LIG3-mediated gap suppression might require repriming activities mediated by Polα, PRIMPOL or another unknown primase, resulting in small gaps that depend on LIG3 to be filled. Upon loss of LIG3, recruitment of MRE11 by CHD4 leads to unscheduled processing of the small gaps into longer stretches of post-replicative ssDNA, resulting in RF stalling and increased genomic instability. PARPi-sensitive BRCA1-deficient cells exhibit post-replicative PARPi-induced ssDNA gaps, which are mediated by 53BP1. Accumulation of PARPi-induced post-replicative ssDNA gaps mediated by 53BP1 and by loss of LIG3 underlies PARPi hyper-sensitivity of BRCA1/LIG3 double-deficient cells. PARPi-resistant BRCA1/53BP1 double-deficient cells lack 53BP1-mediated gap formation, and PARPi-induced ssDNA gaps only occur upon loss of LIG3, resulting in accumulation of longer stretches of post-replicative ssDNA, RF stalling, genomic instability, and PARPi sensitivity.

KEY RESOURCES TABLE

REAGENT or RESOURCE	SOURCE	IDENTIFIER
Antibodies		
Rabbit polyclonal anti-PARP1	Cell Signaling	Cat#9542, RRID:AB_2267956
Rabbit polyclonal anti-LIG3	Sigma-Aldrich	Cat#HPA006723, RRID:AB_1847781
Mouse monoclonal anti-LIG3 [1F3]	Genetex	Cat#GTX70143, RRID:AB_372134
Rabbit polyclonal anti-53BP1	Abcam	Cat#ab21083, RRID: AB_302845
Mouse monoclonal anti-PAR (10H)	Millipore	Cat#AM80, RRID: AB_2155072
Rabbit polyclonal anti-Phospho Histone H2A.X (Ser139)	Cell Signaling	Cat#2577;RRID: AB_2118010
Rabbit polyclonal anti-RAD51	Abcam	Cat#ab133534, RRID:AB_2722613
Mouse polyclonal anti-P53	Monosan	Cat#MONX110194
Rat monoclonal anti-BrdU/CldU [BU1/75 (ICR1)]	Abcam	Cat#ab6326, RRID: AB_305426
Mouse monoclonal anti-BrdU/IdU (B44)	BD	Cat#347580, RRID: AB_400326
Rabbit polyclonal anti- α/β-Tubulin	Cell Signaling	Cat#2148S, RRID:AB_2288042
Mouse monoclonal anti-β-Actin	Sigma	Cat#A5441, RRID:AB_476744
Goat polyclonal anti-rabbit, HRP conjugated	DAKO	Cat#P0448, RRID:AB_2617138
Rabbit polyclonal anti-mouse, HRP conjugated	DAKO	Cat#P0260, RRID: AB_2636929
Goat polyclonal anti-mouse, Alexa Fluor 488- conjugated	Invitrogen	Cat#A11001, RRID: AB_2534069
Goat polyclonal anti-rabbit, Alexa Fluor 488-conjugated	Invitrogen	Cat#A27034, RRID:AB_2536097
Goat polyclonal anti-rabbit, Alexa Fluor 568-conjugated	Invitrogen	Cat#A11011, RRID: AB_143157
Goat polyclonal anti-rat, Alexa Fluor 594- conjugated	Invitrogen	Cat#ab150168
Donkey polyclonal anti-rat Cy3	Jackson Immuno-Research Laboratories, Inc	Cat#712-166-1530, RRID: AB_2340669
Biological samples		
Triple negative breast cancers	(Gogola et al., 2018)	N/A
Human ovarian serous carcinomas	(Moudry et al., 2016)	N/A
Chemicals, peptides, and recombinant proteins		
Olaparib (AZD2281), PARP inhibitor	Syncom, Groningen, the Netherlands	CAS: 763113-22-0
Talazoparib (BMN-673)	Selleckchem	Cat#S7048
PARG inhibitor	Tocris	PDD 0017273; 5952
Veliparib (ABT-888)	Selleck	Cat#S1004
Methyl methanesulfonate (MMS)	Sigma-Aldrich	Cat#129925
4-Hydroxytamoxifen (4-OHT)	Sigma-Aldrich	Cat#H6278
Alt-R® S.p. Cas9 Nuclease 3NLS	IDT	Cat#1081058
Mirin	Sigma-Aldrich	Cat#M9948
Doxycyclin	Sigma-Aldrich	Cat#D9891
ART558	Artios Pharma (Zatreanu et al., 2021)	N/A

REAGENT or RESOURCE	SOURCE	IDENTIFIER
Critical commercial assays		
Click-iT EdU Alexa Fluor 488 Imaging Kit	Invitrogen	Cat# C10337
MitoTracker™ Red CMXRos	Invitrogen	Cat#M7512
Subcellular Protein Fractionation Kit	Thermo Scientific	Cat#78840
Cell Titer Blue	Promega	Cat#G8081
PCR Lentivirus Titration Kit	Applied Biological Materials	Cat#LV900
Experimental models: Cell lines		
KP (a.k.a. KP-3.33)	(Evers et al., 2008)	N/A
KB1P.S (a.k.a. KB1P-G3)	(Jaspers et al., 2013)	N/A
KB1P.R (a.k.a. KB1PM5 ola-res)	(Jaspers et al., 2013)	N/A
ORG-KB1P.S (a.k.a. ORG-KB1P4.N1)	(Duarte et al., 2018)	N/A
ORG-KB1P.R (a.k.a. ORG-KB1P4.R1)	(Duarte et al., 2018)	N/A
ORG-KP (a.k.a. ORG-KPM1)	(Duarte et al., 2018)	N/A
KB1P.S+hB1 (a.k.a. KB1P-G3 *BRCA1* rec)	(Barazas et al., 2019)	N/A
KB1P.R #B1 (wt/mut)	This paper	N/A
KB1P.R #A3 (mut/mut)	This paper	N/A
KB1P.R #F5 (mut/mut)	This paper	N/A
$R26^{CreERT2};Brca1^{SCo/-};Trp53^{-/-}$ mESC (ESP; ES-B1P.R)	This paper	N/A
$R26^{CreERT2};Brca1^{SCo/-}; Trp53^{-/-};Trp53bp1^{-/-}$ mESC (ESP.R; ES-B1P.R)	This paper	N/A
SUM149PT	ATCC	RRID:CVCL_3422
HEK293FT	ATCC	RRID:CVCL_6911
RPE1-hTERT $TP53^{-/-}$ (RPE1-P)	(Noordermeer et al., 2018)	N/A
RPE1-hTERT $TP53^{-/-};BRCA1^{-/-}$ (RPE1-B1P.S)	(Noordermeer et al., 2018)	N/A
RPE1-hTERT $TP53^{-/-};BRCA1^{-/-};TP53BP1^{-/-}$ (RPE1-B1P.R)	(Noordermeer et al., 2018)	N/A
DLD1	Horizon Discovery	RRID:CVCL_0248
Experimental models: Organisms/strains		
Mouse: FVB/NRj	Janvier Labs	N/A
Oligonucleotides		
see Table S2 for sgRNA and primer sequences	This paper	N/A
siCtrl (non-targeting siRNA)	Ambion	Cat#4390843
mouse siLIG3	Ambion	Cat#s69230
human siLIG3 #1	Ambion	Cat# s8177
human siLIG3 #2	Ambion	Cat# s8178
Recombinant DNA		
shRNA DDR-targeting library (TRCMm1.0, lentiviral)	(Xu et al., 2015)	N/A
Plasmid: pLKO.1-scrambled shRNA (lentiviral)	(Xu et al., 2015)	N/A

REAGENT or RESOURCE	SOURCE	IDENTIFIER
Plasmid: pLKO.1-*Lig3* shRNA #1 (mouse, lentiviral)	Sigma Mission Library, TRCMm1.0	TRCN0000070978
Plasmid: pLKO.1- *Lig3* shRNA #2 (mouse, lentiviral)	Sigma Mission Library, TRCMm1.0	TRCN0000070982
Plasmid: pLKO.1- *Rev7* shRNA (mouse, lentiviral)	Sigma Mission Library, TRCMm1.0	TRCN0000006570
Plasmid: pLKO.1-*LIG3* shRNA #1 (human, lentiviral)	Sigma Mission Library, TRC_2 (human)	TRCN0000048498
Plasmid: pLKO.1- *LIG3* shRNA #2 (human, lentiviral)	Sigma Mission Library, TRC v2.0 (human)	TRCN0000300259
Plasmid: pX330-U6-Chimeric_BB-CBh-hSpCas9	(Cong et al., 2013)	Addgene#42230
Plasmid: pX330-U6-Chimeric_BB-CBh-hSpCas9 *Trp53* sgRNA	This paper	N/A
Plasmid: lentiGuide-Puro (lentiviral)	(Sanjana et al., 2014)	Addgene #52963
Plasmid: lentiGuide-Puro (non-targeting) NT sgRNA (lentiviral)	This paper	N/A
Plasmid: lentiGuide-Puro *Trp53bp1* sgRNA This paper (lentiviral)	This paper	N/A
Plasmid: lentiGuide-Puro *Parp1* sgRNA This paper (lentiviral)	This paper	N/A
Plasmid: PCW57.1	N/A	Addgene#41393
Plasmid: PCW57.1 human αLIG3 WT	This paper	N/A
Plasmid: PCW57.1 human αLIG3^{R31L} This paper	This paper	N/A
Plasmid: PCW57.1 human αLIG3 $^{774-922}$ This paper	This paper	N/A

Software and algorithms

MAGeCK	(Li et al., 2014)	N/A
DESeq2	(Love et al., 2014)	N/A
ImageJ software64	(Rueden et al., 2017)	N/A
Cell Profiler software version 3.1.5	(McQuin et al., 2018)	N/A
TIDE (Tracking of Indels by Decomposition)	(Brinkman et al., 2014)	N/A
TIDER (Tracking of Insertions, DEletions and Recombination events)	(Brinkman et al., 2018)	N/A
Benchling [Biology Software]. (2019).	Retrieved from https://www.benchling.com	N/A
ScanR Analysis Software	Olympus	N/A
Tibco spotfire software	(TIBCO Spotfire ®)	N/A
ImageJ macro for the analysis of DNA-damage induced foci	(Xu et al., 2015)	N/A
SynergyFinder	(Ianevski et al., 2020)	N/A
IncuCyte ZOOM 2018A	IncuCyte®	N/A

Deposited data

Raw and uncropped data	This paper; Mendeley	https://doi.org/10.17632/d2t837shk9.1